

Multipactor Threshold Estimation Techniques Based on Circuit Models, Electromagnetic Fields, and Particle Simulators

PABLO GONZÁLEZ ¹, CARLOS ALCAIDE ¹, RAÚL CERVERA ², MIGUEL RODRÍGUEZ ², ÓSCAR MONERRIS ², JOHN PETIT ², ANA RODRÍGUEZ ¹, ANA VIDAL ¹ (Member, IEEE), JOAQUÍN VAGUE ¹, JOSÉ V. MORRO ¹ (Member, IEEE), PABLO SOTO ¹ (Member, IEEE), AND VICENTE E. BORJA ¹ (Fellow, IEEE)

(Invited Paper)

¹ITEAM, Universitat Politècnica de València, 46022 Valencia, Spain

²European High Power Radiofrequency Space Laboratory, Val Space Consortium, 46022 Valencia, Spain

CORRESPONDING AUTHOR: Pablo Soto (e-mail: pabsopac@com.upv.es).

The work of Pablo González was supported by the FPU Fellowship of the Ministerio de Educación, Cultura y Deporte, Spanish Government, with Ref. FPU17/02901. This work was supported in part by the Ministerio de Ciencia e Innovación (MICIN, Spanish Government) under R&D Project PID2019-103982RB-C41 (funded by MICIN/AEI/10.13039/501100011033), and in part by the European Space Agency (ESA) under Project H2020-ESA-007 (funded by the European Union's Horizon 2020 Research and Innovation Program).

ABSTRACT Multipactor has become a keylimiting factor of the final performance of satellite communication systems, due to the increase in power levels and/or operating frequency bands. As a result, the critical components of these systems must meet demanding multipactor specifications which should be considered during the design process. This paper describes the different techniques available to predict the multipactor threshold power for radio frequency (RF) and microwave passive hardware under continuous wave (CW) excitation, from cumbersome particle simulations to fast approximate methods based on circuit models. All these techniques have been described and compared together for the first time, including also a detailed description of the configuration issues of commercial particle simulators required to obtain accurate multipactor threshold predictions. The techniques are applied to both wideband and narrowband application examples. The predictions have been compared with measured thresholds of manufactured samples obtained with a novel multipactor test bed, thus allowing to highlight the advantages and limitations of each technique and particle simulator. From this paper, it will be possible to choose the most suitable procedure (and an appropriate simulator, if needed) to obtain multipactor threshold prediction of passive hardware.

INDEX TERMS High-power design, microwave filters, multipactor, particle tracking simulators, passive circuits, transmission lines, vacuum breakdown.

I. INTRODUCTION

Multipactor discharge [1]–[5] occurs when free electrons, inside a device operating under vacuum conditions, get accelerated and synchronized with the radio frequency (RF) fields; in such a way that the primary electrons impact against the walls of the component with a kinetic energy high enough to release, on average, more than one secondary electron. When this occurs, the electron population increases exponentially and, eventually, a discharge occurs. The discharge can happen on

a single surface or between two surfaces [6], [7]. Multipactor discharges can result in several harmful effects. Some of these effects are: heating of the device walls, increase of reflected power and noise floor, detuning of resonant cavities, outgassing, and physical damages in the device structure [6], [8]. It is believed that some highly damaging corona discharges are ignited by outgassing originating from a multipactor discharge [9]. Multipactor can occur in a wide variety of systems and applications. This paper focuses on RF and microwave

components designed to operate in space [10], [11], but this problem can also appear on klystrons [12], magnetrons [4], [13], particle accelerators and many other devices, that can also be analyzed with the same techniques presented in this work.

Nowadays, the transmitted power in satellite communications is increased as much as possible to improve the performance, as the coding and modulation schemes achieve maximum transmission speeds near the theoretical maximum established by the Shannon theorem [9]. Furthermore, higher transmission rates can be achieved by increasing the channel bandwidth, which is normally accomplished by pushing up the operating frequency of the system. This implies a reduction of the wavelength, thus leading to satellite component miniaturization. It is indeed the case of High Throughput Satellites (HTS), which has moved the operation band from traditional Ku-band to Ka-band or even beyond [14], [15]. The combination of size miniaturization, together with the increase of transmitted signal power, implies electromagnetic (EM) fields of higher intensity inside the device. Power handling issues are therefore, nowadays, a key limiting factor of the system performance. In view of this increasing relevance, having access to fast and accurate multipactor threshold prediction tools, is of paramount importance for the RF and microwave components design process for satellite applications.

Traditionally, multipactor analysis have relied on charts obtained from experimental results (Woode and Petit [16], Woo [17]) for particular geometries. The Woode and Petit charts [16], widely used in practice, were obtained for continuous wave (CW) excitation and parallel-plate like structures, and has also been employed to define a safe multipactor limit in the European and American standards [18], [19]. However, they have proved to provide conservative threshold predictions for most applications, as the parallel-plate case is the geometry providing the lowest multipactor threshold (due to the lack of fringing-field effects pushing electrons away from the critical gap). As a result, applying the corresponding margins implies over-demanding specifications which can increase the cost of the equipment significantly or, alternatively, reduced power levels and therefore a reduction of the potential system throughput.

Particle simulators are able to provide more accurate predictions for a particular geometry, and also allow a wider range of input signals than CW excitation. SPARK3D [20] and CST Particle Studio (CST-PS) [21] have been widely used in the last decade for multipactor analysis [22]–[27]. In recent years, Ansys HFSS [28] has incorporated the capability to perform particle simulations for multipactor threshold estimation. However, the capabilities of HFSS are not analysed in this work because it is not yet as well-established due to its novelty. As it is demonstrated in this paper, the simulation times of these codes are not negligible [29], the correct simulation configuration is cumbersome, and the results interpretation requires some expertise [22].

The main goal of this paper is to provide an in-depth description of the available numerical procedures to

obtain multipactor threshold predictions for RF and microwave passive components. For the first time, several techniques are described and tested to highlight the benefits and drawbacks of each procedure. The direct use of particle simulators, and the combined use of EM simulators and circuit models are considered. Another novelty of this work lies on the multipactor performance comparison between two of the most commonly used particle simulators, in order to provide a reasoned justification of which their application ranges are. The analysis is focused on CW excitation, as this is the most common situation considered in practice and in the technical literature. In addition, dielectric and/or magnetic media is out of the scope of this paper, due to its higher complexity [26], [30]. This paper will therefore contribute to provide guidelines for selecting the most suitable procedure (and the corresponding simulator, if needed) in order to obtain multipactor threshold estimates.

This paper is organized as follows. First, the different techniques that can be applied to obtain a multipactor threshold estimation are presented in Section II. Section III provides an insight on how to perform accurate multipactor threshold predictions using particle tracking simulators. This implies an appropriate configuration and interpretation of the results, which are so often quite involved tasks. Both CST-PS and SPARK3D software packages are considered. The previous theory is applied first to a wideband case in Section IV (coaxial transmission line), and then adapted to perform the analysis of a narrowband device (three-pole combline-like filter) as discussed in Section V. Measured results are reported in Section VI and compared with the predicted thresholds, analyzing the causes of the deviations for each technique and simulator tool. Finally, some concluding remarks are provided in Section VII.

II. MULTIPACTOR THRESHOLD PREDICTION

A. DIRECT PREDICTION

The most straightforward procedure for the computation of the multipactor threshold estimation of an RF/microwave device consists on using a commercial particle simulator on the EM model of the whole component.

Although this is the simplest technique, it has several drawbacks and limitations. As described in more detail in Section III, a particle tracking algorithm needs the knowledge of the EM fields in the structure. The computation of such EM fields can be a cumbersome task, particularly for devices requiring a high meshing density. Structures composed of resonant elements or regions with high-intensity EM fields, that are long in wavelength terms, with narrowband responses or intricate geometrical details are examples of devices implying a high effort in the computation of the EM fields.

On the other hand, a complete structure must be available in order to perform the direct computation of its multipactor threshold. For devices which must fulfill some kind of multipactor specification, this implies the completion of, at least, a preliminary design process before obtaining its multipactor

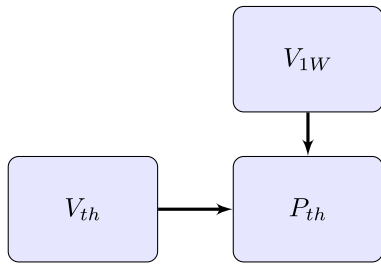


FIGURE 1. Flow diagram of the multipactor threshold prediction based on the critical gap voltage.

performance prediction, and in case it is not the expected one, another complete design cycle must be carried out before performing a new check. This scheme may lead to an increase of the overall design time for complex RF and microwave structures. For these structures, the availability of a procedure to obtain a multipactor threshold estimate at an earlier design stage is of paramount importance. The next subsections describe alternative procedures.

The direct computation of the multipactor threshold is therefore recommended for simple structures in terms of meshing and design time. This explains why most of the direct multipactor threshold predictions available in the technical literature are focused on simple transmission lines, such as a coaxial line (see [25], [29]). In addition, it can also be used to perform the last multipactor check in the final structure, as this technique is the most precise provided that a good enough meshing can be afforded from a computational point of view (in terms of both CPU time and memory). Section III provides key practical guidelines on how to use particle simulators.

B. PREDICTION BASED ON THE CRITICAL GAP VOLTAGE

The prediction technique presented in this subsection, whose flowchart is illustrated in Fig. 1, is based on the previous knowledge of the peak voltage V_{1W} at the multipactor critical gap of the structure.

Exploiting the fact that multipactor is a voltage-driven effect, the peak voltage in the critical gap for a CW excitation at the device input port of 1 W of mean power, V_{1W} , can be combined with the peak voltage level required for a discharge, V_{th} , to predict the multipactor threshold power (in this work all of the predicted thresholds are expressed as the input mean power):

$$P_{th} = 1 \text{ W} \cdot \left(\frac{V_{th}}{V_{1W}} \right)^2. \quad (1)$$

The first step in the procedure is to compute the peak voltage inside the critical gap. This voltage can be obtained by employing different methods. For simple structures, such as transmission lines, the voltage can be obtained analytically as shown in Section IV. For more complex devices, it involves an electromagnetic simulation of an EM model of the real

structure. The voltage must be computed for a given CW excitation, and then scaled to 1 W of input mean power.

The peak threshold voltage V_{th} can be obtained from charts or by using reported experimental data. The most widely used chart is based on a multipactor measurement campaign performed on a parallel-plate like geometry [16]. However, there are charts for other usual geometries, such as a coaxial gap [17], a dielectric-loaded parallel-plate gap [31] or a ridge/multiridge gap [32]. It is important to stress that the threshold voltage, V_{th} , also depends on the material of the surfaces involved in the multipactor discharge.

The main benefit of this technique is the avoidance of the particle tracking simulation to obtain the multipactor threshold prediction. The critical gap voltage V_{1W} must be obtained with an electromagnetic simulator for most of the structures, thus involving a computational effort which may be high for complex devices. However, the requirements of the meshing are only related to the EM field convergence in the critical gap. In this case, further meshing refinements for improving the electron tracking simulation are not required. In addition, it is possible to use a frequency domain solver for a single frequency CW excitation.

The drawback of this approach is the reduction of the accuracy, mainly related to the precision of the peak threshold voltage V_{th} used. This value is normally obtained from available charts or experimental data obtained for some kind of multipactor critical gap, which probably will show some differences with the critical region under consideration. In any case, a conservative estimate can always be obtained by using the lower multipactor limit of the ECSS (European standard) [18], [33] or the Aerospace (USA standard) charts [19] based on a parallel-plate like topology.

C. PREDICTION BASED ON TIME-AVERAGED STORED ENERGY

The procedure based on obtaining the critical gap voltage V_{1W} in Section II-B also implies the availability of an EM model of the entire structure. It is therefore still unsuitable for those components whose complete design is a demanding task, being microwave filters the most representative example. In such cases, a different approach can be envisaged to estimate V_{1W} without requiring the complete design of the structure, which is based on the more complex workflow illustrated in Fig. 2.

The key idea behind this procedure is based on exploiting the time-averaged stored energy (TASE) in a region of the structure including the critical gap. The TASE denotes the summation of the mean electric and magnetic stored energies during a cycle of the CW excitation. For the resonance frequency, the electric and magnetic reactive effects cancel out, resulting in the same electric and magnetic stored energies [34]. Proceeding in this way, the peak voltage V_{1W} at the critical gap can be estimated from the knowledge of the peak gap voltage, V_{1J} , for a time-averaged stored energy (TASE) of 1 J inside a region of the structure including the critical gap, and the time-averaged stored energy $TASE_{1W}$ at such a region for a CW excitation of 1 W of mean power at the input port of

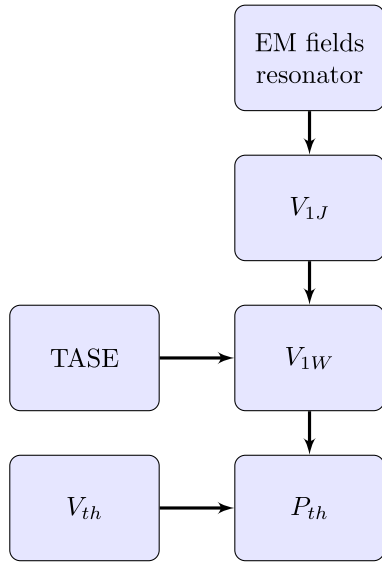


FIGURE 2. Flow diagram of the multipactor threshold prediction based on time-averaged stored energy.

the complete structure:

$$V_{1W} = V_{1J} \cdot \sqrt{\frac{TASE_{1W}}{1J}} \quad (2)$$

so that, after substituting (2) into (1):

$$P_{th} = 1W \cdot \left(\frac{V_{th}}{V_{1J}}\right)^2 \cdot \frac{1J}{TASE_{1W}}. \quad (3)$$

The multipactor discharge in filters is normally originated in a resonator gap, due to the presence of high-intensity EM fields. In such a case, the analysis region can be limited to the isolated resonator including the critical gap. The proposed procedure alleviates the computational burden as it only requires the simulation of a single resonator, instead of considering the whole structure. In addition, the design of an isolated resonator is much simpler and faster than the design of the complete filter, thus reducing the effort to obtain a multipactor threshold prediction. The resonator dimensions can, therefore, be adjusted at an early stage to match the desired multipactor performance.

In order to compute the gap voltage V_{1J} , an eigenmode analysis of the critical resonator is normally used. An eigenmode solver is usually quite fast and accurate, and provides the resonator central frequency and EM fields. The critical gap of the isolated resonator must be maintained in the design of the complete filter. In the case of using the CST eigenmode solver, the EM fields are computed for a total averaged stored energy inside the resonator of 1 J. No scaling factor is therefore required, and V_{1J} is directly obtained from a line integral along the gap:

$$V_{1J} = \left| \int \vec{E} \cdot d\vec{l} \right| \quad (4)$$

where $d\vec{l}$ is the differential line element along the line crossing the critical gap.

The gap voltage V_{1J} of the isolated resonator provides the local information of the critical gap. The information of the whole structure in (3) is included in the parameter $TASE_{1W}$, which represents the time-averaged stored energy of the resonator including the critical gap for a mean power excitation of 1 W at the input port. The TASE takes into consideration how the stored energy distributes along the resonators according to the response and topology chosen for the filter, and can be computed from an equivalent circuit model of the filter. The TASE value in the circuit nodes does not depend on the slope parameter of each resonator, so the conventional normalized version of the coupling matrix \mathbf{M} can be used with all the capacitors C_i set to 1 (see Fig. 3).

First, for a filter of order N , the admittance matrix of the circuit prototype (\mathbf{Y}_{CP}) is obtained from the $N+2$ coupling matrix and the normalized angular frequency ω' [35], [36]:

$$\mathbf{Y}_{CP} = \mathbf{G} + j\omega' \mathbf{C} + j\mathbf{M} \quad (5)$$

where \mathbf{G} is an $N+2$ square matrix whose elements are zero, except for $G_{0,0}$ and $G_{N+1,N+1}$ which represent the source admittance G_S and the load admittance G_L , respectively. \mathbf{C} is a diagonal $N+2 \times N+2$ matrix formed by the array $[0 \ 1 \ 1 \ \dots \ 1 \ 0]^T$ representing the capacitors of the low-pass circuit prototype, \mathbf{M} is the coupling matrix, and ω' denotes the usual frequency transformation:

$$\omega' = \frac{1}{\Delta} \left(\frac{\omega}{\omega_0} - \frac{\omega_0}{\omega} \right) \quad (6)$$

being $\Delta = (\omega_2 - \omega_1)/\omega_0$ and $\omega_0 = \sqrt{\omega_1\omega_2}$ the relative bandwidth and the center angular frequency of the filter pass-band, which extends from ω_1 to ω_2 .

The next step is to compute the voltage at each circuit node (i.e., resonator and input/output ports). They can be easily obtained from the excitation current at each node:

$$\mathbf{V}_{CP} = \mathbf{Y}_{CP}^{-1} \cdot \mathbf{I}_{CP} \quad (7)$$

where \mathbf{V}_{CP} and \mathbf{I}_{CP} are column vectors of $N+2$ elements including the peak voltage and excitation current at each node of the circuit prototype, respectively. For a CW excitation of 1 W of mean power at the input port, the only non-zero element of the vector \mathbf{I}_{CP} is the first one, whose peak value is given by:

$$I_{CP,0} = \sqrt{8G_S}. \quad (8)$$

Finally, the TASE of the i -th resonator node can be computed as the stored energy in the corresponding capacitor ($W_{CP,i}$) multiplied by a scale factor depending on the frequency transformation (6) for the filter under study [34]:

$$\begin{aligned} TASE_{1W,i} &= W_{CP,i} \frac{d\omega'}{d\omega} \\ &= \frac{|V_{CP,i}|^2 C_i d\omega'}{4 d\omega} \end{aligned}$$

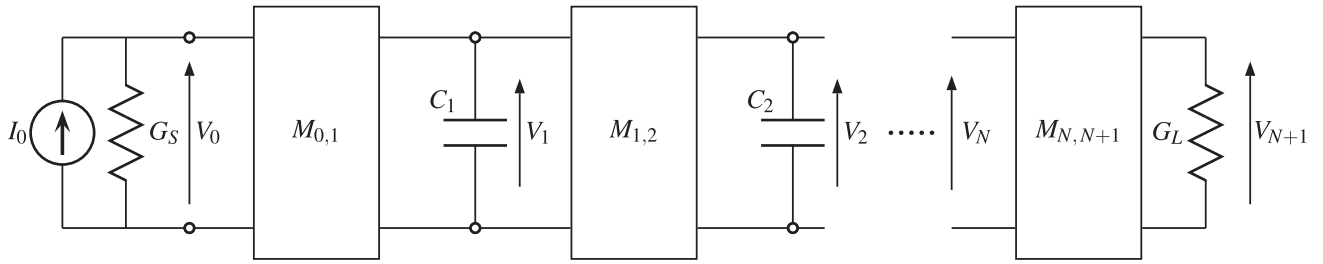


FIGURE 3. Generic in-line low-pass circuit prototype (shunt configuration) of an N order filter.

$$= \frac{|V_{CP,i}|^2}{4\Delta} \left(\frac{1}{\omega_0} + \frac{\omega_0}{\omega^2} \right). \quad (9)$$

For filters composed of resonators with a similar gap, the TASE distribution of the circuit prototype nodes identifies the resonator with a higher stored energy and, therefore, more prone to suffer a multipactor discharge. The identification of the critical resonator depends on both the particular geometry of each resonator, and the distribution of the TASE in the circuit nodes.

Once the parameters V_{1J} and the $TASE_{1W}$ at the critical resonator are obtained, the multipactor threshold for the whole structure can be obtained from (3).

This method is slightly less accurate than the one described in Section II-B, since the critical gap peak voltage V_{1W} is estimated using the information extracted from the circuit prototype and an isolated resonator, instead of using the complete structure. For instance, it does not account for the effect of the resonator coupling elements in V_{1J} . However, it usually provides a good multipactor threshold estimate without requiring the EM model of the complete structure, thus allowing the control of the multipactor performance of the structure at the first design stages (i.e., during the design of the isolated resonators). This is an outstanding advantage in high-power filter design, as it can result in a dramatic time reduction when compared with a trial and error procedure requiring a complete design of the structure before performing each multipactor threshold prediction.

III. PARTICLE SIMULATOR CONFIGURATION

The direct method of obtaining a multipactor threshold estimation described in Section II-II-A is based on the use of a particle simulator on an EM model of the structure. This prediction method is normally performed at least once, in order to carry out a final check of the multipactor performance of the designed component. An in-depth description of the simulation set-up, and a discussion on how and why the most important configuration parameters affect the predicted thresholds, are provided in this section.

The generic simulation flow of multipactor direct prediction is shown in Fig. 4. A particle tracking simulation requires having access to the EM fields of the structure, the excitation signals, the electron seeding characteristics, and the secondary emission yield (SEY) values of the surfaces involved in the

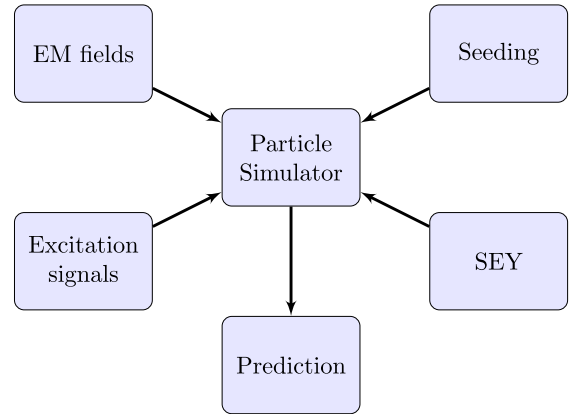


FIGURE 4. Flow diagram for a generic multipactor direct prediction.

multipactor discharge. The simulations consist in injecting a number of electrons (seeding electrons) inside the structure, which are accelerated by the EM fields. Particle simulators compute the electron trajectories, detecting if and when the electrons collide with the walls, and evaluating from the wall surface SEY how many secondary electrons are released in these collisions. As a result, the electron population evolution with time is obtained, which can be used to infer the multipactor threshold prediction.

Although the EM fields are computed externally to the particle tracking code, they are of paramount importance in the accuracy and computational efficiency of the multipactor analysis. The use of a tetrahedral or hexahedral meshing for obtaining the EM fields can play in fact a significant role. The tetrahedral meshing is very adaptive and, therefore, well-suited for structures with small details (i.e, arbitrary shapes, rounded corners and coaxial feedings) and regions with very high EM fields (i.e, sharp corners with high fringing fields). Moreover, the meshing should be dense enough in the particular regions where multipactor is expected to happen, in order to obtain an excellent local representation of the EM fields. This allows an accurate computation of the electron trajectories and, therefore, a more precise estimation of the multipactor threshold. In many cases, the meshing needed to get convergent multipactor results is more dense than the one required for S-parameter convergence. However, producing such a dense mesh in the overall structure is normally

inefficient, as for multipactor simulation purposes it is only necessary around the critical gap.

The electron seeding carried out inside the structure is also of high relevance. The main parameters of the seeding are the number of seeding electrons, how they are distributed in the seeding region, and the initial velocity distribution (in magnitude and direction) of the electrons. The energy of the seeding electrons should be low (of a very few eV), as they must be accelerated by the EM fields. The effect of the other seeding parameters is discussed in this section, being the most important one the electron seeding density in the critical region. As electron tracking simulators perform an statistical analysis, a minimum density is required to obtain convergent results (that barely change for different simulations performed with the same configuration parameters).

The SEY of the walls around the vacuum region are also of outermost relevance. The SEY of a surface represents the mean number of electrons emitted after the impact of a primary electron on a surface, which depends on the impact energy and incidence angle of the primary electrons, and also on the characteristics of the surface (material, finish, roughness, etc.). Note that an average SEY greater than one is required to sustain a multipactor discharge. The SEY characteristic curve (depending on the primary electrons impact energy) has a very strong effect on the multipactor threshold. There are models which define the SEY in terms of the primary electrons energies using a limited number of parameters, being the Vaughan model the most widely known [37]. In spite of the availability of tables of usual values for the Vaughan parameters of typical materials [33], a more accurate representation is obtained by means of SEY measurement campaigns. Measurement of the SEY curve, however, is a cumbersome and difficult task, and the SEY values may be uncertain at times. This complexity is highly increased for dielectric and magnetic media surfaces. Moreover, SEY values are also affected by aging. In fact, the uncertainties in the SEY characteristics may explain, in many cases, most of the discrepancies between measured and predicted thresholds.

The next subsections provide a detailed description for each of the two particle tracking simulators under consideration in this paper, SPARK3D and CST-PS. Table 1 summarizes the main differences between both software tools. HFSS has some similarities with SPARK3D, as it also uncouples the field computation (steady-state EM fields) from the particle tracking simulation. It is worth mentioning that some companies, such as major suppliers of microwave equipment for satellites, have developed in-house tools which can also be used to evaluate the multipactor threshold of microwave devices (in some cases, by linking a commercial particle simulation tool to its own proprietary software).

A. SPARK3D SIMULATION CONFIGURATION

1) FIELD COMPUTATION

SPARK3D needs to be fed with EM fields computed using an external software package (FEST3D, CST Microwave Studio

(CST-MWS) or Ansys HFSS), as SPARK3D is exclusively a particle simulator. In particular, it requires steady-state EM fields obtained from a frequency domain solver. The number of mesh cells used barely affects the execution speed of the SPARK3D simulation (once the EM fields have been imported), as the software performs an internal interpolation to compute the fields at each location of the multipactor analysis region defined by the user. However, it has a significant impact on the execution speed of the external frequency domain solver required to obtain the EM fields of the structure. A very important concept linked to the accuracy of the field computation is the meshing concept. The meshing refers to the decomposition of the structure geometry in polyhedrons. The electromagnetic solver computes the EM fields at the vertices of such polyhedrons, which can be used to interpolate the fields at any point of the structure. The quality and density of the mesh, and therefore of the input EM fields, impacts on the accuracy of the computation of the electron trajectories.

2) SIGNAL DEFINITION

Different signal types can be defined in SPARK3D:

- 1) Continuous wave (CW) signal.
- 2) Pulsed signal.
- 3) Multicarrier with different amplitude/phase carriers.
- 4) Modulated signal on a single carrier.
- 5) Multicarrier with a different modulated signal for each carrier.

In this work only the CW excitation is explored. Here, it is worth mentioning that SPARK3D performs the normalization for a mean Root Mean Square (RMS) power of 1 W. Therefore, the input power specified by SPARK3D when showing simulation results makes reference to mean power.

3) ELECTRON SEEDING AND REGION LIMITATION

Particle simulations rely on the Montecarlo statistical principle. Therefore, the number and characteristics of the seeding electrons are key parameters in the simulation configuration. SPARK3D allows the user to define a parallelepiped region where the multipactor analysis will be performed, so that any electron that goes through the boundaries of such a region is discarded by the simulator. Restricting the analysis region is highly recommended (when possible) for two reasons: the simulation is more efficient as only the electrons in the critical region are tracked, and a high electron seeding density is achieved in the analysis region with the same number of seeding electrons (improving the statistical performance of the simulation).

The seeding electrons can be placed uniformly within the seeding volume, or can be distributed non-uniformly by placing more electrons in the locations with higher EM field densities. Generally speaking, the non-uniform (used by default) seeding is advantageous, as placing electrons in the most multipactor-prone regions (in case the user is unable to identify them) implies the electrons are present in high field regions straightaway, hence reducing the execution time.

TABLE 1. Comparison of SPARK3D and CST-PS Main Features

Feature	SPARK3D	CST-PS	Differences
EM fields computation	Imported from external software (CST Microwave Studio, Ansys HFSS or FEST3D). Only frequency domain.	The natural approach is time domain based, using an FDTD technique operating simultaneously to the PIC solver.	For band limited devices, frequency domain approaches are preferred over time domain ones. Hexahedral meshing of FDTD is less efficient than tetrahedral one to represent geometric details and regions with higher-intensity EM fields.
Secondary emission	Modified Vaughan and raw imported data.	Vaughan, Furman-Pivi and Import-Vaughan.	SPARK3D allows a Modified Vaughan model whereas CST-PS implements a Furman-Pivi model. CST-PS does not distinguish elastically backscattered electrons when raw data (measurements) is imported.
Electron seeding	Maxwellian in a user defined volume. No re-seeding possible.	Maxwellian in a user defined volume. Re-seeding possible.	The distributions of the initial velocities of seeding electrons in CST-PS and SPARK3D are not directly comparable.
Simulation region	It can be bounded by the user (being the same where the seeding is carried out).	It is always the whole structure.	SPARK3D allows the user to limit the simulation to the critical region, increasing the computational efficiency.
Macroparticles	Automatic electron grouping (and ungrouping) into macroparticles.	User can specify number of electrons per macroparticle, which is fixed for all the simulation.	Different operation principles. CST-PS is significantly slower for high populations (being unable to handle populations in excess of 10^7 macroparticles). The use of a higher number of electrons per macroparticle is possible, but the macroparticle density must be kept above recommended limits to not degrade the statistical performance.
Space charge effects	Not included.	Space charge can be enabled or disabled.	CST-PS provides a higher flexibility. For instance, it allows to compute the variation in the reflected signal due to the multipactor effect (which is also observed in multipactor testing).
Detection criterion	Three different types. Suitable for all signal scenarios.	Only one type, valid only for CW and multicarrier signals.	Moreover, SPARK3D has an automated power loop algorithm providing the multipactor threshold prediction within a user defined accuracy.

However, this way of proceeding can be problematic if the analysis region is affected by intense fringing fields. The fringing fields tend to take the electrons out of the critical region, so most of the seeding electrons placed in zones with fringing fields will be unproductive, leading to a higher risk of an artificial increase of the predicted threshold.

4) SEY DEFINITION

SPARK3D provides three different options for the SEY definition:

- 1) SEY curve obtained from a modified Vaughan model with parameters E_1 , E_{\max} , SEY_{\max} and SEY_{low} [38].
- 2) Introduce measured SEY data using an ASCII file.
- 3) Use of the predefined SEY curves provided by SPARK3D, based on a modified Vaughan model for a range of typical materials.

In addition, SPARK3D allows the user to define independent SEY values for both elastically reflected electrons (for

low-energy impacts) and true secondary electrons, in order to distinguish electrons having different emission characteristics [38], [39]. SPARK3D (from version 2021 onwards) allows the user to define a different curve to describe the SEY of each of the materials included in the simulation model, so that the SEY behaviour of each of the considered materials can be characterized independently.

5) THRESHOLD DEFINITION

The multipactor criterion is used to decide whether discharge happens or not for a given input mean power. For SPARK3D, three different options are available.

- 1) **Charge trend:** SPARK3D fits the electron evolution to an exponential curve (for a specific signal interval), and checks whether there is positive or negative growth. It is the faster method, although may suffer from higher variability.

- 2) **Charge (fixed factor):** the number of electrons must increase over the initial number of electrons by a factor, set by the user, to consider a discharge happens. There is a risk of long simulations taking place, since the population must drop to zero to discard a discharge.
- 3) **Charge (automated factor):** similar to the charge (fixed factor), but the factor (both for considering or discarding a discharge) is set automatically by the software depending on the simulation time (it is higher at the beginning of the simulation to reduce the risks of false detection). Only available for CW excitation.

The default criterion for CW signals is the charge (automated factor), for multicarrier signals is the charge trend (using the multicarrier signal period), whereas for modulated signal the charge (fixed factor) is used.

B. CST-PS SIMULATION CONFIGURATION

1) FIELD COMPUTATION

CST-PS performs the particle tracking simulation in the time domain using an hexahedral meshing. However, the EM fields used for the simulation can be obtained in two different ways. The first one uses the CW fields computed by the frequency domain solver of CST-MWS (similarly to SPARK3D), which are loaded as external steady-state fields and finally interpolated into the CST-PS hexahedral meshing. The second method consists in a full time domain simulation, where CST-PS computes the time evolution of the fields following a finite-difference time-domain (FDTD) approach [40] simultaneously with the electron dynamics simulation. As a result, any arbitrary time domain waveform can be used as excitation, although an appropriate time delay to vanish the transient is required for a steady-state CW simulation. This second method is the default and more natural option for CST-PS. It is worth pointing out that, in contrast to SPARK3D, CST-PS is able to evaluate the effect of the particles in the EM fields, referred to as space charge effect [41]. However, this effect does not seem relevant in the ignition of a discharge and, therefore, in the multipactor threshold prediction, being normally deactivated to increase the computational efficiency [42].

For the full time domain simulation scheme used by CST-PS, the mesh density has a severe impact on the computation time, as it implies the calculation of the EM fields at a larger number of positions at each time step for each power level. In addition, for narrowband hardware as filters, the time steps must be very small (so that the representation of the EM field evolution in the structure is accurate), significantly increasing the computational cost. For such cases, frequency domain techniques are normally best-suited [43]. Note also that, in contrast to frequency domain approaches, simulation errors accumulate with time. Moreover, the time domain hexahedral meshing used by CST-PS does not seem to be as effective as a tetrahedral one, due to the limitations in meshing flexibility inherent to FDTD approaches, so a much higher number of mesh cells is required to reach the same level of accuracy.

This is particularly true for complex structures with arbitrary geometries, or regions with very intense EM fields.

2) SIGNAL DEFINITION

CST-PS has different ways for defining input signals:

- 1) Using a predefined signal type (such a sine step).
- 2) Importing an ASCII table with the time domain signal.
- 3) Defining a custom signal through an external Visual Basic interface.

A scaling factor is used in CST-PS to specify the power of the excitation signal to be applied at the input port. An amplitude of 1 implies a peak power of 1 W for the whole signal, which represents a mean power of 0.5 W for the particular case of a CW signal excitation.

3) ELECTRON SEEDING AND REGION LIMITATION

CST-PS does not allow to limit the simulation to a particular part of the structure, so an electron which moves away from the critical region is tracked along the whole structure (therefore increasing the simulation time). However, CST-PS allows the user to constrain the seeding to a particular region of the structure (with circular, cylindrical or rectangular shape), so that the seeding electrons can be launched in the critical region in order to improve the seeding density and the statistical performance. To the best of the authors' knowledge, CST-PS places the seeding electrons uniformly along the seeding region. CST-PS does also provide different seeding mechanisms, allowing continuous seeding from given surfaces or points (this operating mode can be useful in some particular cases). CST-PS also allows the user to specify the seeding instant (or instants), which can be used to compensate time delay effects in the structure response.

Both CST-PS and SPARK3D make use of macroparticles. A macroparticle is a particle with the mass and electrical charge of several electrons, which is tracked as a single particle by the particle simulator. In fact, the basic simulation unit for CST-PS is a macroparticle composed of as many electrons as the user specifies in the seeding menu, being this a fixed amount for all the multipactor simulation. Defining several electrons per macroparticle allows analysing a higher number of electrons with the same computational resources. However, as each macroparticle is tracked as a single particle, the statistical performance is related to the number of macroparticles instead of the number of electrons. As a result, the multipactor threshold may be increased if the density of seeding macroparticles in the critical region is not high enough. SPARK3D follows a different approach, as it dynamically groups and ungroups electrons into macroparticles, in order to keep a suitable balance between particle density (i.e., statistical performance) and computational resources (CPU time and memory usage) throughout the simulation.

4) SEY DEFINITION

CST-PS provides three different ways for defining the SEY of a material:

TABLE 2. Dimensions of the Coaxial Transmission Line Under Consideration

D_{in}	2.476 mm	Inner conductor diameter
D_{out}	5.7 mm	Outer conductor diameter

- 1) The user can introduce E_1 , E_{max} and SEY_{max} to generate the corresponding Vaughan model [37].
- 2) The user can introduce the SEY data using an ASCII file (for instance, measured SEY data).
- 3) The user can introduce the parameters for the Furman and Pivi model [44].

For the option in which the user introduces the SEY data from a text file (for instance, from measurements), all the SEY values are attributed to true secondary electrons. Therefore, the main SEY contribution at low impact energies, the one related to elastically reflected electrons, cannot be specified.

It is not possible to completely replicate a CST-PS multipactor configuration in SPARK3D and vice-versa, since the characteristics of the released secondary electrons (initial energy, phase and direction) do not follow the same distributions. However, and in contrast to SPARK3D, CST-PS allows the user to modify the statistical mode of the energy distribution used for the secondary electrons emitted when the primary electrons collide against the material surfaces.

5) THRESHOLD DEFINITION

For CST-PS only one criterion for multipactor detection is available. This criterion is very similar to the charge trend method of SPARK3D. In this case, the user also sets the minimum growth factor, the interval length, and the number of consecutive intervals which must satisfy the growth factor condition to consider multipactor. This criterion is valid for CW and multicarrier excitation, provided that the interval length is chosen to be equal to an integer multiple of the signal period.

IV. WIDEBAND APPLICATION

The first case of study is a simple uniform section of a coaxial transmission line in vacuum. The multipactor analysis of coaxial lines has been studied exhaustively by means of analytical [45], [46], numerical [41], [47], [48] and experimental methods [17], [46]. Since the gap voltage in this type of transmission line can be easily computed, the fast approach in Section II-B is followed first. Next, the direct prediction approach from Section II-A (considering all configuration details in Section III) is used to highlight the particularities of the simulation configuration flows in both CST-PS and SPARK3D.

The dimensions of the transmission line are included in Table 2, resulting in a characteristic impedance Z_0 of 50 Ω . The length is not specified as it does not affect the prediction of the multipactor threshold. The material of the metal walls is assumed to be Aluminum. A 3D view of the coaxial geometry is shown in Fig. 5.

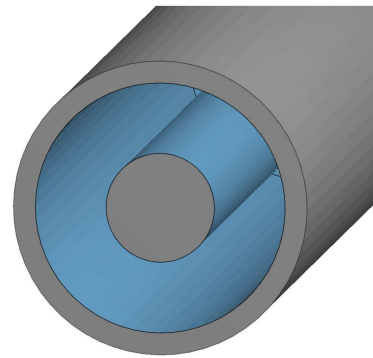


FIGURE 5. Coaxial transmission line in vacuum.

TABLE 3. Multipactor Peak Threshold Voltage V_{th} (in V) for the Coaxial Line at Different Frequencies From Available Charts

Frequency (GHz)	0.75	0.83	1	1.35	1.575	3.5
$f \times d$ (GHz·mm)	1.21	1.34	1.61	2.18	2.54	5.64
ECSS limit (Al)	39	48	65	88	103	228
ECSS theory (Al)	44	53	76	140	188	320
Woo (Cu)	57	63	84	127	155	-

A. CIRCUIT MODEL APPROACH

The peak voltage V between the two conductors of a TEM transmission line can be easily computed from its characteristic impedance Z_0 , by using the well-known formula:

$$P = \frac{V^2}{2Z_0}. \quad (10)$$

For an input mean power P of 1 W, the formula in (10) can be rearranged to provide V_{1W} as follows:

$$V_{1W} = \sqrt{2Z_0} \quad (11)$$

which yields a value of 10 V for V_{1W} by taking $Z_0 = 50 \Omega$ for the wideband coaxial line.

An alternative procedure to obtain the value of V_{1W} is to perform a line integral of the electric field in an appropriate EM model of this structure. It is advisable to perform this simple check before carrying out a particle tracking simulation, in order to ensure that the results obtained with different prediction techniques are consistent.

On the other hand, the multipactor peak threshold voltage V_{th} of the coaxial line under consideration can be obtained from available charts. Table 3 includes this information for the lower conservative limit and the theoretical curves of the ECSS calculator for Aluminum [49], and from the data reported by Woo for a coaxial line of 50 Ω made of copper [17]. In Table 3, d is the well-known gap distance, in this case the one between the inner and outer conductors (of diameters D_{in} and D_{out} , respectively) of the coaxial line (i.e., $d = (D_{out} - D_{in})/2$). Taking into account that the work of Woo did not provide data for Aluminum surfaces, the theoretical curve provided in the ECSS calculator fitted to measured data (ECSS theory) has been used to derive, by using (1),

TABLE 4. Predicted Multipactor Threshold Mean Power P_{th} for the Coaxial Line at Different Frequencies

Frequency (GHz)	0.75	0.83	1	1.35	1.575	3.5
P_{th} (W)	19.4	28.1	57.8	196	353.4	1024

TABLE 5. SPARK3D Predicted Thresholds at 1.5785 GHz for Different Electron Seeding Density, and for Default and Homogeneous Seeding Cases

Seeding electrons	Density (e/m^3)	Default (W)	Homogeneous (W)
		1.5785 GHz	1.5785 GHz
10000	$1.2 \cdot 10^{10}$	249.7	249.7
1000	$1.2 \cdot 10^9$	249.7	249.7
100	$1.2 \cdot 10^8$	267.2	254.1
10	$1.2 \cdot 10^7$	>1e6	371.1

the predicted mean power level for the multipactor threshold shown in Table 4.

B. PARTICLE SIMULATION APPROACH

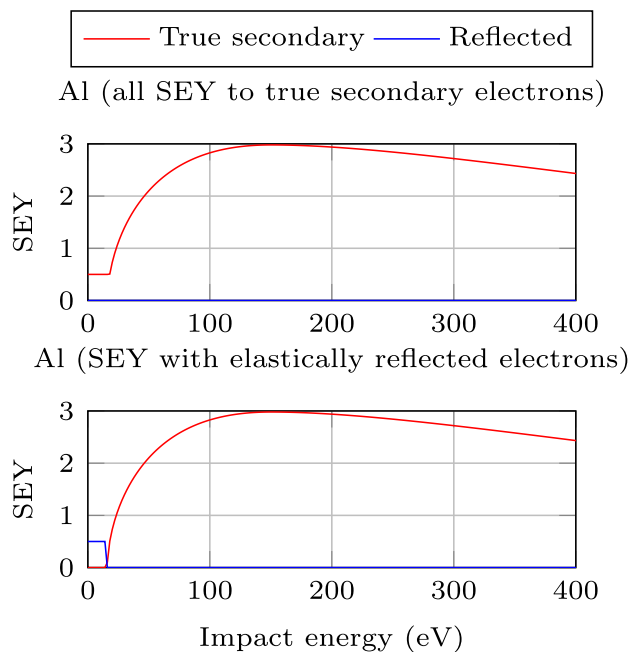
1) SPARK3D SIMULATION

First, the SPARK3D simulation results are provided. The default discharge criterion of SPARK3D for CW signals is used to consider when a multipactor event occurs. The SEY curve for both metal conductors is a modified version of the default ECSS Aluminium SEY file provided by SPARK3D, where all the SEY values (including the ones for the low impact energy region) are assigned to true secondary electrons. This makes possible a more fair comparison with CST-PS. Note that CST-PS considers that all imported SEY data are due only to true secondary electrons.

For the above configuration, the predicted thresholds at 1.5785 GHz for a different number of seeding electrons are compiled in Table 5. Both the default inhomogeneous (non-uniform) seeding and the homogeneous (uniform) seeding have been considered.

From the results included in Table 5, it can be inferred that the number of seeding electrons can have a significant impact on the predicted threshold. Fully convergent results are obtained for an electron seeding density above $10^9 e/m^3$ in the analysis region. A lower electron density impairs the statistics causing an artificial increase in the multipactor threshold power, particularly for values below $10^8 e/m^3$. The seeding type does not make a great difference in this case, due to the lack of fringing fields. However, as the seeding density decreases, the homogeneous seeding seems to be more stable (in terms of multipactor threshold prediction) than the default one.

The automatic threshold determination process for these simulations in SPARK3D takes about one and a half hours, after requiring nine simulations with different power levels. The EM fields computed by the frequency domain solver of CST-MWS are obtained in just a few minutes. A 10-core Intel i9-10900X with a clock frequency of 3.70 GHz and 256 GB of RAM has been used, although it must be taken into account

**FIGURE 6.** Comparison of normal incidence SEY curves without (top plot) and with (bottom plot) elastically reflected electrons at the low range of primary electron impact energy (blue line).

that the SPARK3D simulation only uses one core and requires a limited amount of RAM memory. Even though the prediction based on a circuit approach is immediate, the time effort with SPARK3D is not very demanding due to the simplicity of the wideband structure. It is important to point out that for all of the SPARK3D simulations the threshold determination precision is set to 0.1 dB to get accurate results. However, for many practical applications a precision of 0.5 dB can be enough. In the latter case, the execution time may reduce to a few minutes.

In order to check the sensitivity of the CW multipactor threshold to the type of modelling for the low energy impacts, the default ECSS Aluminum SEY characteristic of SPARK3D is considered as well (where the SEY in the low energy range, of value 0.5, is assigned to the elastically reflected electrons). A plot comparing the two SEY curves used, for an impact energy range between 0 and 400 eV, is provided in Fig. 6. The red traces correspond to the true secondary electrons, whereas the blue traces correspond to the elastically reflected electrons. The case with no elastically reflected electrons has a blue trace whose values are all zero, whereas the red curve integrates the SEY value of the ECSS Aluminum of SPARK3D originally assigned to elastically reflected electrons.

The results in Table 6 for a convergent seeding (this is ensured by using 10000 seeding electrons with an homogeneous distribution, in line with the information in Table 5) shows a slight reduction of 0.13 dB in the multipactor threshold level, which can be explained by the fact that for elastic impacts the electrons do not lose energy (for true secondary electrons, the material absorbs part of the primary electron impact energy).

TABLE 6. SPARK3D Predicted Thresholds at 1.5785 GHz for Case With SPARK3D ECSS Aluminum and SPARK3D ECSS Aluminum With No Elastically Reflected Electrons

SPARK3D ECSS Aluminium (W)	242.2
No elastically reflected (W)	249.7
Difference (dB)	0.13

TABLE 7. SPARK3D Predicted Thresholds for Different Frequencies, and Difference (Delta in dB) of the Circuit-Based Approach Thresholds (In Table 4) to the Ones Obtained by SPARK3D

Frequency (GHz)	0.75	1.35	1.575	3.5
$f \times d$ (GHz·mm)	1.21	2.18	2.54	5.64
Predicted threshold (W)	25.6	173.4	251.8	1071.8
Delta circuit (dB)	-1.20	0.53	1.47	-0.20

TABLE 8. CST-PS Predicted Thresholds for Different Statistical Modes of the Gamma Energy Distribution of the Released Secondary Electrons at 1.5785 GHz

Energy mode (eV)	1	2	3	4	5	7.5
Threshold (W)	324	240	200	170	150	118

The low energy region is more relevant for multicarrier or modulated signal excitations, where some parts of a signal causing a discharge can be below the CW multipactor threshold.

Finally, the predicted threshold of SPARK3D for different frequency-gap product values are provided in Table 7. For these simulations, 10000 seeding electrons and the homogeneous seeding are used again.

From Table 7, it is possible to infer that the thresholds obtained with the circuit-based approach (see Table 4) agree reasonably well with the ones predicted by SPARK3D for all the frequency-gap product cases considered. As a result, they can be used as a preliminary fast estimate of the multipactor threshold for the wideband structure.

2) CST-PS SIMULATION

A further validation is conducted via CST-PS simulation. The same SEY curve used in SPARK3D is imported in CST-PS. An experienced user decides, based on the electron population evolution, if a multipactor discharge is ignited (following a similar criterion to the default one used by SPARK3D).

A relevant difference between SPARK3D and CST-PS tools is that the latter one can define the statistical mode of the gamma distribution used for the energy of the secondary electrons. This parameter has a significant impact on the multipactor threshold, as shown in Table 8 (using 10000 seeding electrons). The default value used by CST-PS is 7.5 eV. This value can be appropriate for some applications (i.e., particle accelerators, klystrons) but is too large for multipactor effect. A value of about 2 eV seems to provide a better agreement to SPARK3D predictions. The authors have checked that this value also provides a good agreement with measured data available in the literature for other geometries. SPARK3D

TABLE 9. CST-PS Predicted Thresholds at 1.5785 GHz for Different Number of Seeding Electrons

Seeding electrons	Density (e/m^3)	Homogeneous (W)
		1.5785 GHz
10000	$1.2 \cdot 10^{10}$	239.5
1000	$1.2 \cdot 10^9$	240.0
100	$1.2 \cdot 10^8$	241.0
10	$1.2 \cdot 10^7$	245.0

TABLE 10. CST-PS Predicted Thresholds for Different Frequencies (in GHz · mm), and Differences (Delta in dB) of Circuit-Based and SPARK3D Predicted Thresholds to the Ones Obtained by CST-PS

Frequency (GHz)	0.75	1.35	1.575	3.5
$f \times d$ (GHz·mm)	1.21	2.18	2.54	5.64
Predicted threshold (W)	25.8	142.6	238.0	960.5
Delta circuit (dB)	-1.22	1.38	1.71	0.28
Delta SPARK3D (dB)	-0.03	0.85	0.24	0.48

does not allow the user to modify this parameter, but it also employs a low energy range for the released true secondary electrons even though a different statistical distribution is used. For the remaining CST-PS simulations reported in this paper, the parameter governing the energy distribution of the true secondary electrons has been fixed to 2 eV.

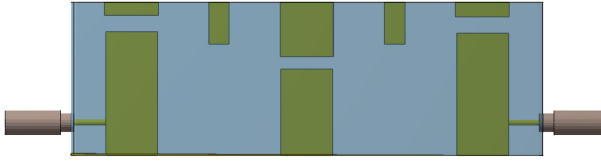
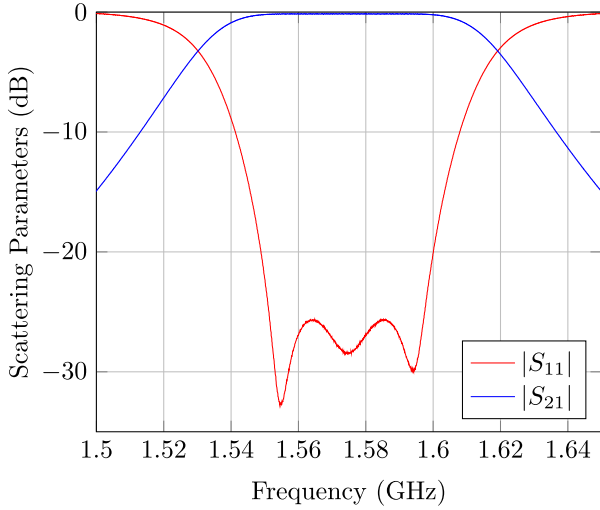
A convergence analysis on the electron seeding density has also been carried out at the frequency of 1.5785 GHz. As it can be seen in Table 9, CST-PS is able to provide convergent results with a seeding density one order of magnitude lower to the one required by SPARK3D, thus allowing a reduction in the number of seeding electrons.

For the configuration with 1000 seeding electrons (with a similar number of mesh cells to the one used in SPARK3D), a simulation using a power level close to the critical value lasts around 45 minutes in the same 10-core Intel i9-10900X platform, but now using its whole computing capabilities. If nine simulations with different power levels are to be performed, the simulation time needed to obtain a threshold would take a few hours. This is becoming a significant amount of CPU time resources for a relatively simple wideband structure, although still within reasonable limits.

With the object of providing an exhaustive analysis on how different factors affect the multipactor threshold predictions, the change in the predicted thresholds for different frequency-gap products is provided in Table 10. As it can be seen, there is a good agreement between CST-PS and SPARK3D predictions, although it seems that CST-PS is slightly more conservative for the mode of 2 eV chosen for the energy of the true secondary electrons.

V. NARROWBAND APPLICATION

The third-order filter in Fig. 7 is the case of study selected for this section. It consists in a combline-like filter with posts of square section in the filter body and lid, which are coupled by proximity, and with small inter-resonator posts of also square cross-section. The input and output ports are TNC connectors,


FIGURE 7. Layout of the combline-like filter for the narrowband case.

FIGURE 8. Measured S-parameter response of the manufactured combline prototype filter.

whose central pins are in electrical contact with the first and last resonator posts.

The original filter specifications are a pass-band of 50 MHz centered at 1.5754 GHz with a return loss of 23 dB (to guarantee a return loss goal of at least 20 dB after manufacturing). The filter was manufactured, and only the first and last resonator were tuned by inserting a screw at the center of the corresponding lid posts. The central resonator, as well as the input/output and inter-resonator couplings were not tuned, resulting in a pass-band center frequency of 1.5743 GHz and a bandwidth of 45.7 MHz. In the filter pass-band, the return loss and insertion loss were, respectively, better than 25 dB and lower than 0.18 dB. The measured S-parameters of the manufactured filter are shown in Fig. 8.

A. CIRCUIT MODEL APPROACH

For this particular example, the procedure described in Section II.II-C is followed to obtain the multipactor threshold prediction. The main advantage of this method is that it can be applied before the actual filter is fully designed, thus allowing to obtain a fast estimate of the multipactor threshold. This value can be used to refine the structure in an early design stage, in order to fulfill the power-handling specifications for the final device. As a result, it avoids the use of the direct prediction technique (see Section II.II-A) until the final version of the filter is designed, and the last multipactor check is to be performed.

TABLE 11. TASE for Each Resonator Node at 1.548 and 1.575 GHz

Frequency	Resonator 1	Resonator 2	Resonator 3
1.548 GHz	2.6179 nJ	4.0867 nJ	2.1019 nJ
1.575 GHz	2.1761 nJ	3.1648 nJ	2.0957 nJ

For comparison purposes, the procedure is applied for a filter which recovers the measured S-parameter response of the manufactured structure. In an actual design process of a filter, the S-parameters of the goal response must be used instead, from which the coupling matrix can be built theoretically [50]–[52].

The only gaps in which multipactor can happen inside this structure are the ones between the lower and upper posts of each resonator. The TASE of the equivalent circuit nodes provides information on the distribution of energy in the filter resonators. Using CST Filter Designer, it is easy to extract the actual coupling matrix of the filter structure from the measured response:

$$\mathbf{M} = \begin{pmatrix} 0 & 1.31 & 0 & 0 & 0 \\ 1.31 & -0.01 & 1.32 & 0 & 0 \\ 0 & 1.32 & -0.01 & 1.35 & 0 \\ 0 & 0 & 1.35 & -0.03 & 1.29 \\ 0 & 0 & 0 & 1.29 & 0 \end{pmatrix}. \quad (12)$$

Once the coupling matrix is determined, the next step is to build the admittance matrix for the circuit prototype. In the case of a bandpass filter, it is necessary to incorporate the frequency mapping (6) into (5) obtaining:

$$\mathbf{Y}_{CP} = \mathbf{G} + \frac{j}{\Delta} \left(\frac{f}{f_0} - \frac{f_0}{f} \right) \mathbf{C} + j\mathbf{M} \quad (13)$$

where the matrices \mathbf{G} , \mathbf{C} and \mathbf{M} are the same ones defined previously in Section II.II-C. The elements of such matrices are included in the equivalent circuit of Fig. 3 (where all capacitors C_i are set to 1).

At this point, the computation of voltage in each node of the circuit prototype is straightforward through (7). Then the TASE of each resonator retrieved from (9) can be rewritten in terms of frequency as:

$$TASE_{1W,i} = \frac{|V_{CP,i}|^2}{8\pi\Delta} \left(\frac{1}{f_0} + \frac{f_0}{f^2} \right) \quad (14)$$

being $f_0 = \sqrt{f_1 f_2}$ the center frequency of the filter pass-band, which extends from f_1 to f_2 .

It is important to note that the TASE is highly frequency-dependent, as can be seen in Fig. 9. The TASE at 1.548 GHz (close to the lower band edge frequency of the pass-band) and at 1.575 GHz (close to the pass-band center frequency) are collected in Table 11.

According to Table 11, the resonator node with higher stored energy is the central one. In case that all the resonators have nearly the same geometry for the critical gap (a usual situation in practice), it should be the one with higher EM fields.

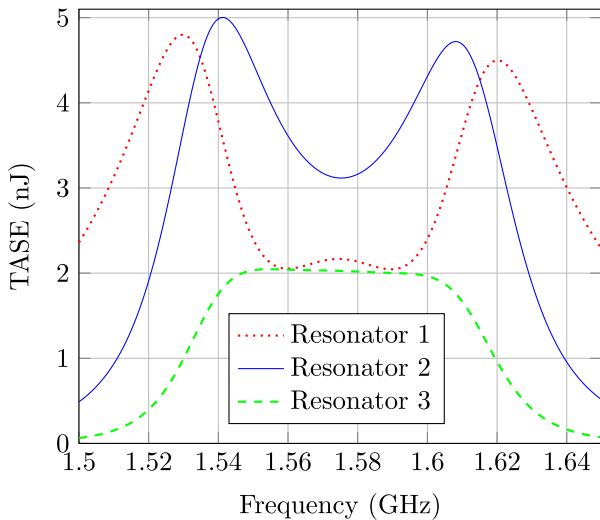


FIGURE 9. TASE in each resonator of the third-order combline filter in terms of the frequency.

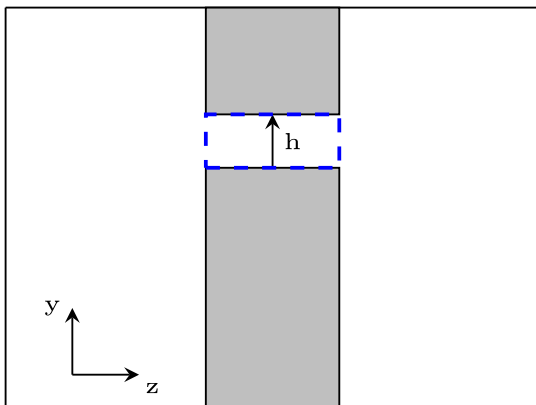


FIGURE 10. Model of the isolated second resonator. The critical gap is enclosed by the dashed blue box.

For the filter under consideration, moreover, it has been designed to have a narrower gap in the central resonator (3.6 mm vs 4.6 mm in the first and last resonator). Considering that the highest TASE value and the smallest gap correspond to the second resonator, one can conclude that the second resonator should be the critical one (i.e., the most multipactor-prone resonator).

From the previous discussion, it turns out to be evident that the resonator where we have to compute the gap voltage V_{IJ} for 1 J of stored energy is the central one. An EM model of the isolated central resonator has been developed (see Fig. 10), and analyzed by using the CST Eigenmode Solver. This simulation takes less than 2 minutes in the Intel i9-10900X platform and provides accurate results. It is important to remark that the critical dimension of the gap (i.e. the height) must be the real one, whereas other dimensions of the resonator must be slightly modified to match the central frequency of the resonator in the filter (compensating the absence of the loading effect related to the inter-resonator coupling).

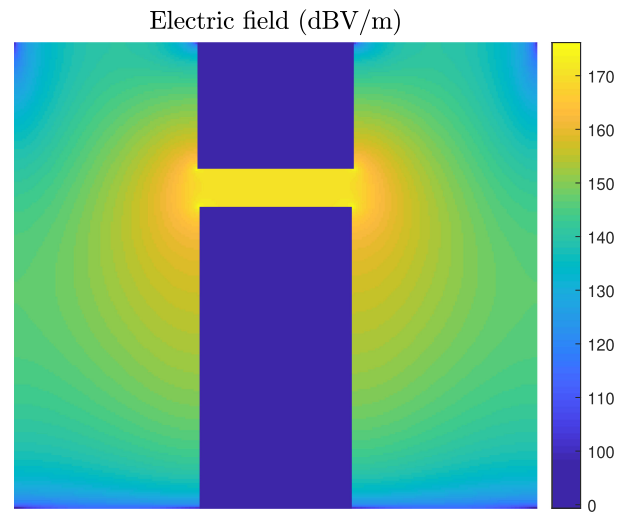


FIGURE 11. Electric field in the second resonator computed with CST Eigenmode Solver for 1 J of total time-average stored energy.

TABLE 12. Comparison of V_{1W} Values Obtained With the Approximate Method Using the Isolated Resonator Model and the Circuit TASE (IR + TASE), and the Numerical Method Simulating the Whole Structure With the Frequency Domain Solver of CST-MWS

Frequency	IR + TASE	CST-MWS	Error
1.548 GHz	82.30 V	91.84 V	0.95 dB
1.575 GHz	72.42 V	74.94 V	0.30 dB

After the computation of the electric field as shown in Fig. 11, the line integral along the critical dimension of the gap (see Fig. 10) is performed, giving the V_{IJ} as:

$$V_{IJ} = \left| \int_h E_y dy \right| \quad (15)$$

where E_y is the y component of the electric field, and dy is the differential line element also in the y direction. Computing the line integral from (15) with CST-MWS, the value of the voltage along the y direction of the gap is $V_{IJ} = 1.2874 \cdot 10^6$ V.

Now, following the steps from the flowchart in Fig. 2, the value of V_{1W} can be obtained by combining V_{IJ} and the TASE for the second resonator through (2), yielding 82.30 V and 72.42 V for 1.548 GHz and 1.575 GHz, respectively. The value of V_{IJ} computed at the filter center frequency has been used for both frequencies, as the field distribution inside the resonator for a 1 J stored energy would be quite similar at the relatively narrow filter pass-band.

Since an EM model of the manufactured filter matching the measured S-parameter response is available, it is possible to check the accuracy of the method followed to obtain V_{1W} . Table 12 compares the value of V_{1W} computed combining the TASE and V_{IJ} , and the one obtained by performing the numerical integral from a frequency domain simulation of the whole structure carried out in CST-MWS. As it can be seen, the agreement is excellent at both frequencies under consideration, and particularly for 1.575 GHz. Since the frequency of 1.548 GHz is slightly outside the filter pass-band, the EM field

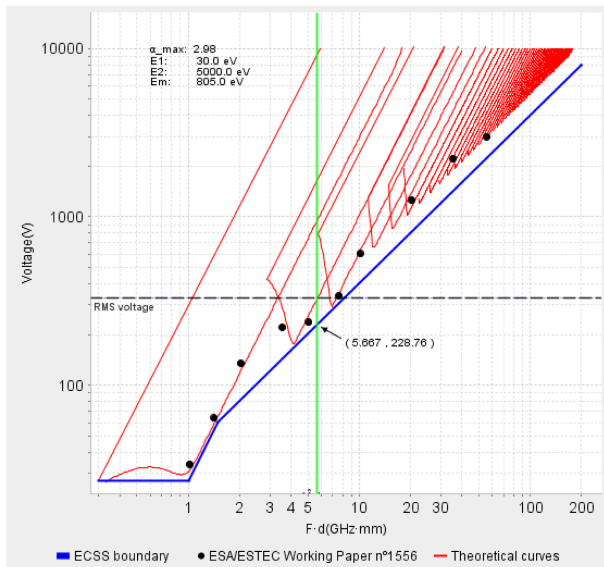


FIGURE 12. Evaluation of the multipactor threshold of the filter at 1.575 GHz with the ECSS calculator.

distribution in the resonator can be slightly different to the one at the central frequency, thus explaining the slight increase in the discrepancies.

The next step is to obtain the threshold voltage in the critical gap. Since the critical gap is quite similar to a parallel-plate one (the side of the resonator post is more than 4 times longer than the gap height), the Woode and Petit charts [16] can be used to find the corresponding threshold voltage. The use of the ECSS calculator for 1.575 GHz is illustrated in Fig. 12. The conservative ECSS limit for such a frequency is $V_{th,ECSS\ limit} = 228.8$ V, whereas for the red curve (fitted to measured data) the peak threshold voltage $V_{th,ECSS\ theory}$ increases to about 330 V. Using the last value, and after combining (14) and (3), the multipactor threshold power is computed yielding a value of $P_{th} = 20.4$ W. For 1.548 GHz the predicted threshold drops to $P_{th} = 14.5$ W since $V_{th,ECSS\ theory}$ is about 313 V for such a frequency.

B. PARTICLE SIMULATION APPROACH

Direct particle simulations have been performed in the EM model of the manufactured structure. This model is obtained from the measured physical dimension of the filter body and lid, with some minor adjustments to fit the measured S-parameter response, namely, in the first and last resonator (due to the fine tuning performed by tuning screws) and the input/output couplings. The SEY curve characteristics have been obtained from SEY measurements carried out in the body and lid of the filter at the position of the critical gap in the central resonator. In SPARK3D, all the SEY values have been assigned to the true secondary electrons curve to provide a fair comparison with CST-PS.

TABLE 13. SPARK3D Predicted Thresholds for Different Number of Seeding Electrons and for Default (Inhomogeneous) and Homogeneous Seeding Cases in the Comblin Filter at Frequencies of 1.548 GHz and 1.575 GHz

Seeding electrons	Density (e/m^3)	Default (W)		Homogeneous (W)	
		1.548	1.575	1.548	1.575
10000	$7.0 \cdot 10^9$	12.1	21.4	12.1	19.9
1000	$7.0 \cdot 10^8$	11.9	20.9	12.1	20.1
100	$7.0 \cdot 10^7$	16.1	37.3	12.1	21.1
10	$7.0 \cdot 10^6$	88.6	2.6e6	15.1	31.3

1) SPARK3D SIMULATION

The EM model has been analyzed using the frequency domain solver of CST-MWS. The resulting EM fields at 1.548 GHz and 1.575 GHz are exported to SPARK3D. A mesh of 500 k tetrahedrons, with an increased mesh cell density in the critical gap, has been considered. Using the default discharge criterion of SPARK3D and an analysis region around the critical gap, the predicted thresholds for a different number of seeding configurations are reported in Table 13.

From Table 13, it stands out that for this particular structure the seeding type has a more significant effect. In this case, it is advisable to avoid the use of the default (inhomogeneous) seeding, since it will waste a lot of seeding electrons thrown away from the critical gap, due to the intense fringing fields close to the borders of the resonator posts. For the homogeneous seeding, an electron seeding density above $10^9 e/m^3$ seems enough to get fully convergent results, similarly to the wideband case.

The CPU time was about two hours for 8 simulations with different power levels (for a SPARK3D accuracy of 0.1 dB), with 10000 seeding electrons leading to the multipactor threshold prediction. The computation of the S-parameters and EM fields with the 500 k mesh cells in CST-MWS takes around 7 hours. These results have been obtained in a 3.7 GHz 10-core Intel i9-10900X processor with 256 GB of RAM. These CPU times are still within reasonable limits, and can be handled comfortably using the available computational resources. The main burden is related to obtaining the EM fields, but it must be taken into account that this simulation must be performed only once (and results for additional frequencies can be obtained without a severe CPU time penalty). Moreover, the authors have not tried to reduce the size of the employed meshing as much as possible, which would have led to a reduction of the overall CPU time of the process.

2) CST-PS SIMULATION

A CST-PS simulation is always carried out as a time domain simulation, where the solver computes simultaneously the evolution of the EM fields (independently of the technique used for their computation) and the particle trajectories. However, for narrowband structures, the time domain field computation requires a much denser meshing than the frequency domain computation. In addition, it uses a hexahedral meshing, which is not as well-suited as the tetrahedral one for a resonant structure including regions with high-amplitude EM fields

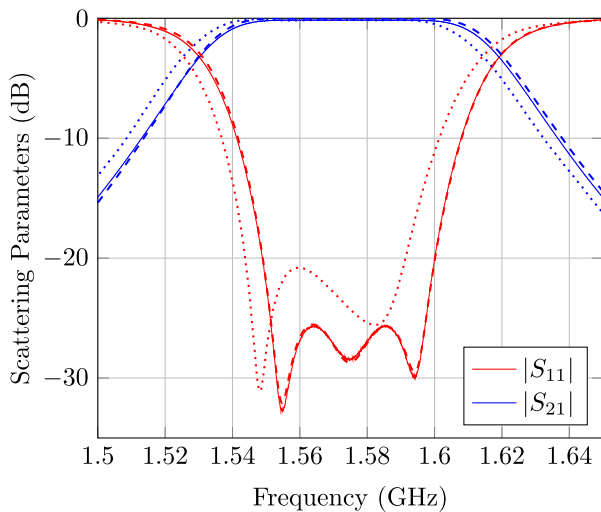


FIGURE 13. Comparison of S-parameters of the combline filter. Solid lines are measured results, whereas dashed and dotted lines are simulated data used by SPARK3D and CST-PS, respectively.

(such as around the sharp edges of the resonator posts). In fact, the time domain meshing was unable to achieve convergence after 10000 k mesh cells (the computational limit for a 10-core Intel i9-10900X with 3.70 GHz clock speed and 256 GB of RAM), although the response was slowly approaching to the one obtained using the CST-MWS frequency domain solver.

Fig. 13 plots the measured S-parameters of the manufactured device, and compares with the simulated response obtained from CST-MWS in frequency domain with a 500 k tetrahedral mesh (used for SPARK3D simulations) and with a 2000 k hexahedral mesh (used for CST-PS simulations). The response of the structure corresponding to the CST-PS simulation has a pass-band with a return loss better than 20.8 dB centered at 1.5672 GHz with a bandwidth of 46.3 MHz. Besides the reduction in the return loss level, there is a downwards frequency shift of 7.1 MHz, which will cause a relevant effect in the multipactor threshold estimation in terms of the CW excitation frequency. Moreover, a 300 ns simulation in CST-PS with this dense mesh takes about 24 hours in the 10-core Intel i9-10900X platform for a single power level, being the computation of the EM fields the more demanding task. This effort must be repeated for each power simulation, in contrast to SPARK3D. All these results reveal the limitations of CST-PS for the simulation of narrowband structures like filters, even for a third-order in-line topology.

Following a similar procedure to the one carried out for the wideband example, where an experienced user decides whether a discharge occurs or not based on the evolution of the electron population, the multipactor threshold was obtained for a different number of seeding electrons. The results for a 1.575 GHz continuous wave (CW) excitation are shown in Table 14. As it can be seen, convergent results are obtained from an electron seeding density in the critical region of about 10^8 e/m^3 .

TABLE 14. CST-PS Predicted Thresholds at 1.575 GHz for Different Number of Seeding Electrons

Seeding electrons	Density (e/m^3)	Homogeneous (W)
		1.575 GHz
10000	$7.0 \cdot 10^9$	14.1
1000	$7.0 \cdot 10^8$	14.1
100	$7.0 \cdot 10^7$	14.3
10	$7.0 \cdot 10^6$	14.4

VI. COMPARISON WITH EXPERIMENTAL RESULTS

In this section, the multipactor threshold predictions for the two examples discussed in Sections IV and V are compared with measured data of manufactured samples. The multipactor test bed and the testing procedures used are described first.

A. EXPERIMENTAL TEST BED AND PROCEDURE

The standard multipactor test bed, as defined in [18], typically uses a pulsed CW signal with an RF ON time of 20 μs and a pulse repetition period of 1 ms. Under these signal characteristics, literature has widely proved that the measured multipactor threshold is identical to the one obtained using a CW signal excitation [16].

The multipactor test bed used in this work (see Fig. 14) was not the standard one, as it was developed to cope not only with CW signals, but also with modulated ones, and to overcome some inherent limitations of traditional multipactor test beds. Anyway, in this particular application, it was used for CW excitation.

Keeping in mind that multipactor is an effect which depends on the material SEY properties, it is of utmost importance to ensure that these properties do not change over time. There is an effect, known as conditioning, which is produced after a long exposure of the device under test (DUT) to continuous multipactor discharges. The main consequence of conditioning is that the multipactor threshold increases due to microscopic changes in the critical gap area, which results in a local variation of the SEY characteristics.

Although the change in the multipactor threshold due to conditioning can be restored by breaking the vacuum, and allowing the DUT to stay at ambient pressure conditions for a few hours, this blocks the test activity for a minimum of 12 hours. To overcome this issue related to conditioning, the advanced multipactor testing technique uses a pulse by pulse testing approach. For this way of testing, a pulse of the signal is transmitted once, and the next repetition is not transmitted until the absence of multipactor in the detection systems has been confirmed. This pulse-by-pulse transmission technique allows to carry out up to 15 different tests per day.

In the schematic of the multipactor test bed shown in Fig. 14, several differences arise with respect to a traditional one. In this case, most of the detection systems (i.e. reverse IQ, harmonic and electron monitoring) operate synchronously. As detailed in [53], a novel in-phase and quadrature method is used to replace the more classical microwave nulling system. All the collected data is gathered in one single control PC,

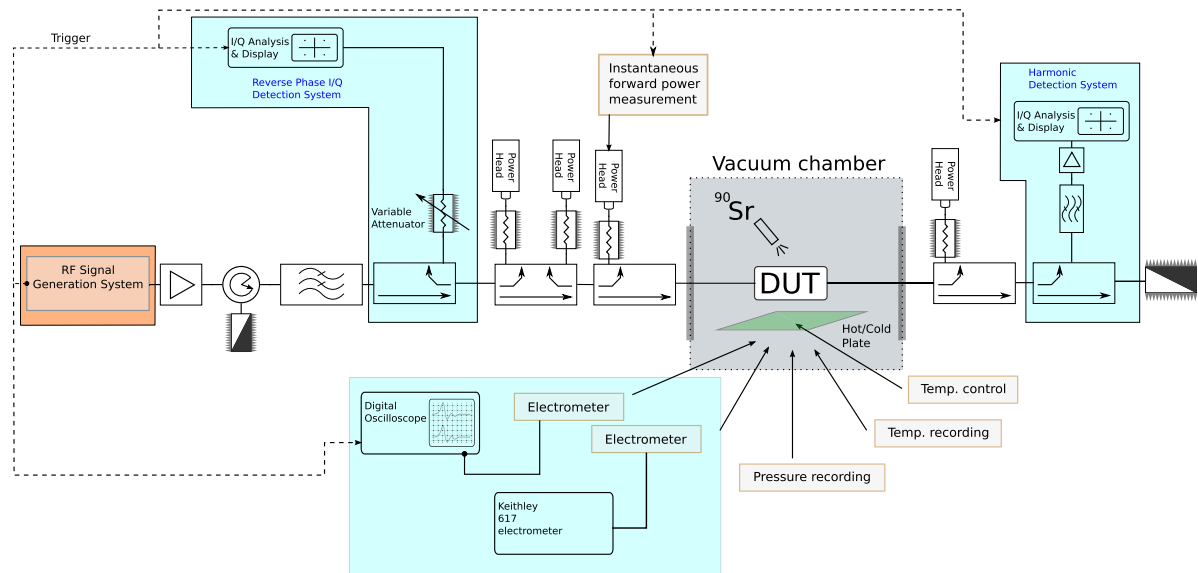


FIGURE 14. Multipactor test bed used to obtain the experimental results. The novel in-phase and quadrature detection method is used in replacement of the input harmonic detection and microwave nulling systems.

and the next signal repetition will not be generated until the previous one has been fully analyzed. From the specifications point of view, the signal generation and acquisition capabilities cover up to 1.25 Gsps, and the power amplifier used for the L-band measurements is a 1 kW CW solid state power amplifier.

The multipactor detection relies on the responses from sensors in the test-bed presented in Fig. 14. When a discharge happens, the multipactor test operator observes a noticeable change in the sensor responses. For this particular test, a change in the response was observed at 12.0 W, at 1548.0 MHz, on the reverse-IQ and electron probe detectors and at 17.8 W, at 1575.0 MHz again on the reverse-IQ and electron probes. No significant responses were observed on the harmonic-IQ detection system, although it should be noted that this could be a less sensitive system due to the inherent harmonic rejection of the filter. The photo multipliers were not available at the time the tests were conducted. These thresholds were confirmed by slightly reducing the applied power to extinguish the discharge and then increasing the applied power again until multipactor occurred. The ECSS criterion for nominating the multipactor threshold level establishes that, at least, two detection techniques must provide clear responses [18], [33]. This criterion has been met for this particular test.

B. RESULTS AND DISCUSSION

The manufactured samples of the two application examples considered in Sections IV and V were measured in the multipactor set-up described in the previous subsection. Table 15 includes the measured multipactor threshold values, and compares them with the predictions using the circuit approach and a direct approach with both SPARK3D and CST-PS.

TABLE 15. Comparison Between Predicted and Measured Multipactor Thresholds for the Coaxial Transmission Line and the 3-Pole Comblin Filter Samples

		Coaxial line		Comblin filter	
Frequency (GHz)		1.575	1.548	1.575	
Measured		220 W	12.0 W	17.9 W	
Circuit Approach	Predicted	353.4 W	14.5 W	20.4 W	
	Delta	2.06 dB	0.82 dB	0.57 dB	
SPARK3D	Predicted	251.8 W	12.1 W	19.9 W	
	Delta	0.59 dB	0.04 dB	0.46 dB	
CST-PS	Predicted	238 W	9.5 W	14.1 W	
	Delta	0.34 dB	-1.01 dB	-1.04 dB	

For the comblin filter, measured SEY data of the critical gap surfaces have been used to obtain the multipactor threshold predictions. The coaxial line is a sample made of copper several years ago, which has been stored in ambient conditions. As the copper may have been oxidized, the typical SEY performance of Aluminum has been used instead.

There is a quite good agreement between the measured results and the ones predicted by the two particle simulation tools under consideration. For the case of SPARK3D, it must be taken into account that all the SEY values have been attributed to true secondary electrons, so that the comparison with CST-PS is more fair. The case in which the low impact energy region is assigned to elastically reflected electrons would have obtained a reduction of about 0.1 dB (for the coaxial line) and 0.3 dB (for the comblin filter) in the SPARK3D predictions, thus reducing the overall differences with the measured multipactor thresholds.

The CST-PS prediction for the coaxial line threshold is also excellent using 2 eV for the mode of the energy distribution of the true secondary electrons (instead of the default value of

7.5 eV). However, the discrepancies for the combline filter are more significant. There are two potential reasons explaining this effect. The main one is the effect of the meshing, which is unable to provide a fully convergent scattering parameter response for the CST-PS simulation with the available computational resources (see Fig. 13). Due to the downwards frequency shift, the test frequencies are not placed slightly below the lower band-edge and close to the pass-band center frequency of the simulated S-parameter response for CST-PS, thus modifying the group delay and therefore affecting the multipactor threshold estimates. Therefore, the predicted threshold of 14.1 W at 1.575 GHz should be slightly lower than the one that would have been obtained at the center frequency of the response (placed around 1.567 GHz), whereas the multipactor threshold of 9.5 W at 1.548 GHz will be even lower if it is computed slightly below the lower band-edge of the simulated pass-band. Therefore, CST-PS tends to underestimate the multipactor threshold in about 1 to 1.5 dB. This difference can be explained by the poorer performance of the hexahedral meshing in the sharp corners of the resonators, which reduces the effect of the fringing fields that take electrons outside of the critical gap, thus leading to an artificial reduction of the predicted threshold. Probably the less exhaustive meshing in these regions also explains the lower convergence rate in the S-parameter response. In addition, for this case a better agreement would have been obtained by setting the parameter of the secondary energy distribution slightly below 2 eV (see Table 8).

The computation of the multipactor threshold by a direct use of a particle simulation tool, however, is time consuming. This is particularly true for a narrowband application (i.e., a filter), where in addition a complete filter topology is required. The circuitual approach described in Sections II-B and II-C provides an alternative method which gives a fast estimate without requiring the use of a particle tracking simulation. In addition to the advantage in terms of time, this technique can be applied during an early design stage, which is particularly important for filters. If the critical gap voltage can be easily estimated, as in a transmission line, the approach in Section II-B should be followed. On the other hand, for more complex structures as filters, the procedure based on the TASE detailed in Section II-C should be used instead. According to Table 15, the prediction obtained by the circuit approach for the filter case is quite accurate, whereas for the coaxial line a deviation of about 2 dB is observed.

The main limitation of the circuitual approach is related to the availability of a representative estimate for the peak threshold voltage V_{th} . This value can be derived from graphs or tables obtained for particular structures and materials. The potential disagreement between the particular case under consideration and the one used to obtain the value of V_{th} will have a clear impact in the prediction accuracy. For the coaxial line under consideration it is possible to use the other two values of V_{th} in Table 3. By using the ECSS limit at 1.575 GHz, $V_{th} = 103$ V and $P_{th} = 106$ W, whereas with the data from Woo measurements $V_{th} = 155$ V and $P_{th} = 240$ W. The first

TABLE 16. Comparison Between Measured and Circuit-Based Multipactor Thresholds Using the ECSS Limit for Aluminum

Frequency (GHz)		Coaxial line	Comblin filter	
Measured		1.575 220 W	1.548 12.0 W	1.575 17.9 W
Circuit	ECSS limit	106 W	7.5 W	10.0 W
Approach	Delta	-3.17 dB	-2.04 dB	-2.53 dB

estimate provides a worst-case prediction based on a parallel-plate topology. The second one is very close to experimental data, but it was obtained from a copper coaxial line of an unknown SEY (while the SEY characteristic of the real sample must be similar to the one of Aluminum because of oxidation). In particular, and according to the ECSS calculator [49], the $f \times d$ region between 2.5 and 3.5 corresponds to a transition band between first- and third-order multipactor, thereby providing a wide margin between the ECSS limit and the value of the theoretical curves fitted to measurements.

In any case, the usual goal from a design point of view is the avoidance of a multipactor discharge for the operation power level of the component. For this particular application, the use of the V_{th} for the worst-case ECSS limit will provide a fast and conservative estimate of P_{th} that can be used to guide the design of the component. Driven by the experience and the characteristics of the critical gap, the designer may also take controlled risks in terms of the power-handling capabilities of the component if needed. Table 16 shows the multipactor threshold predicted by the circuit approach using the peak threshold voltage provided by the ECSS limit, $V_{th,ECSS\ limit}$. As it can be seen, it provides a conservative estimate with is about 2 to 3 dB below experimental results.

From the previous discussion, the designer can extract the guidelines to identify the most suitable approach to obtain a multipactor estimation for a particular application. In case that the multipactor threshold is to be obtained by using directly a particle tracking simulation with an EM model of the structure, the designer should also identify the most appropriate software tool.

Concerning accuracy, both particle tracking simulators show a similar performance, provided that the meshing of the EM model is dense enough to get a fair representation of the EM fields in the structure. The comparison between both simulators, performed in Table 10 for the coaxial line, is quite good for a wide range of frequency-gap products, once the energy of the secondary electrons in CST Particle Studio is properly adjusted. For the narrowband application the differences are somewhat higher (see Table 15), but can be explained by the limitations in the CST-PS meshing, which leads to a device response shifted downwards in frequency. Moreover, SPARK3D may provide thresholds more similar to the measured ones, if the SEY value for the low impact energy region is assigned to elastically reflected electrons instead of true secondary electrons (CST-PS does not provide this option, since all imported SEY values are attributed to true secondary electrons).

In terms of seeding, CST-PS has advantages over SPARK3D, as it obtains fully convergent results with an electron seeding density of 10^8 e/m³, whereas SPARK3D requires an order of magnitude higher. SPARK3D, however, is able to group and ungroup electrons in macroparticles dynamically, thus alleviating the computational cost increase. In any case, the number of electrons that must be tracked to determine the ignition of a multipactor discharge is not high for CW excitation, as only a sustained increase in the electron population is required. Finally, in SPARK3D the user should select the most suitable type of seeding for the particular application (default or homogeneous), whereas the seeding on CST-PS seems to work properly in the narrowband and the wideband applications analyzed thanks to its lower sensitivity to the electron seeding density.

The execution time of CST-PS is normally higher than the one required by SPARK3D, as the EM fields are computed simultaneously to the particle tracking simulation using a FDTD approach (and must be recomputed again for each power level simulation). On the other hand, SPARK3D uncouples the computation of the fields of the particle tracking simulation, resulting in a computational advantage. The differences in CPU time increase substantially for complex narrowband structures of high order, or with geometrical details requiring a finer meshing. In such cases, a tetrahedral meshing (compatible with SPARK3D) outperforms the hexahedral meshing of CST-PS and its limitations. The computational time required by CST-PS for the very dense meshing required can be prohibitive, whereas the meshing size barely affects the simulation time in SPARK3D. Moreover, SPARK3D allows to confine the simulation in a limited region of the structure due to the use of frequency domain steady-state EM fields, thus requiring only the fields of such a critical zone.

According to the results obtained for the third-order combline-like filter, which is a simplified low-order model of a real filter for L-band satellite applications, it seems that CST PS will not be able to perform an accurate multipactor analysis of practical filters (at least, considering the whole structure). Due to computational limitations linked to the meshing of real filters (of moderate and high complexity), it is not possible to obtain convergent results for the EM fields and multipactor effect within reasonable CPU times. In contrast, the CPU time of SPARK3D depends only slightly on the meshing (and a limited analysis region can always be defined), so the main limitation will be the external computation of the EM fields by a frequency domain solver (which is more suitable for moderate and complex filters than a time domain electromagnetic solver).

Last, but not the least, CST Particle Studio is a very general and configurable particle tracking software, able to perform almost any type of simulations (for instance, including effects that change with time, such as the space charge effect related to particle interactions). However, it is less user-friendly and more difficult to configure than SPARK3D. For instance, a CST-PS user must configure several power sweeps before obtaining the multipactor threshold, whereas SPARK3D has a

fully automated procedure for the determination of the threshold, which reduces the time spent by the user to get the final result.

VII. CONCLUSION

This paper has described in detail the different techniques available to predict the multipactor threshold for RF and microwave passive hardware under CW excitation. The direct use of particle tracking simulators with an EM model of the structure has been explored, including a detailed description of the configuration issues to overcome in order to obtain accurate predictions. SPARK3D and CST Particle Studio, the simulation tools traditionally used for multipactor threshold estimation, have been thoroughly compared for wideband and narrowband applications. It has been shown how SPARK3D is suitable for both type of applications, whereas CST Particle Studio has computational limitations for narrowband devices (particularly, for high order filters and/or filters with involved geometries). CST Particle Studio has proved to be more configurable, but at the same time less user friendly than SPARK3D. This is due to the fact that SPARK3D is a tool particularly suited for multipactor analysis, whereas CST Particle Studio is a particle tracking software with a broader application range.

Alternatively, a technique based on a circuit model approach has been proposed. It has been shown that such a technique is able to provide very fast estimates of the multipactor threshold, which can be used at an early stage of the design process. This is particularly important for filters, thus allowing to refine the filter dimensions to fulfill the multipactor specifications before the complete filter with the required response is designed. A particular approach for narrowband structures based on the time average stored energy of a prototype circuit model is described. It allows a reduction in the overall design time required for complex devices involving multipactor requirements.

The predictions have been compared with measured thresholds of two manufactured prototypes by using a novel multipactor test bed. As a result, it has been possible to clearly highlight the advantages and limitations of each prediction technique and simulator in terms of both accuracy and computational efficiency. This paper, therefore, provides the main guidelines on how to effectively choose and use/configure the most suitable technique/simulator to predict the multipactor threshold of passive RF and microwave components.

Furthermore, the use of the simulation techniques discussed in this work may reduce the high safety margins normally added in the power handling specifications, thus leading to a significant cost reduction in the development of microwave equipment [11].

ACKNOWLEDGMENT

The authors would like to thank the European High RF Power Space Laboratory of the European Space Agency and Val Space Consortium for contributing with its installations –

Laboratory co-funded by the European Regional Development Fund— A way of making Europe. The authors would also like to thank the reviewers of the manuscript, whose comments have indeed contributed to improve the final version of the paper. Aurora Software and Testing S.L. (AURORASAT) and CST, now part of Dassault Systèmes are the developers of SPARK3D and CST PS (both currently integrated into CST Studio Suite), respectively. AURORASAT was originally a spin-off company, where some of the authors of this work (belonging to Universitat Politècnica de València) have collaborated with.

REFERENCES

- [1] P. T. Farnsworth, "Television by electron image scanning," *J. Franklin Inst.*, vol. 218, no. 4, pp. 411–444, Oct. 1934.
- [2] E. W. B. Gill and A. von Engel, "Starting potentials of high-frequency gas discharges at low pressure," *Proc. Roy. Soc. A*, vol. 192, no. 1030, pp. 446–463, Feb. 1948.
- [3] A. J. Hatch and H. B. Williams, "Multipacting modes of high-frequency gaseous breakdown," *Phys. Rev.*, vol. 112, pp. 681–685, Nov. 1958.
- [4] J. R. M. Vaughan, "Observations of multipactor in magnetrons," *IEEE Trans. Electron Devices*, vol. 15, no. 11, pp. 883–889, Nov. 1968.
- [5] J. R. M. Vaughan, "Multipactor," *IEEE Trans. Electron Devices*, vol. 35, no. 7, pp. 1172–1180, Jul. 1988.
- [6] R. Kishek, Y.-Y. Lau, L. Ang, A. Valfells, and R. Gilgenbach, "Multipactor discharge on metals and dielectrics: Historical review and recent theories," *Phys. Plasmas*, vol. 5, no. 5, pp. 2120–2126, Apr. 1998.
- [7] G. Torregrosa, A. Coves, C. P. Vicente, A. M. Perez, B. Gimeno, and V. E. Boria, "Time evolution of an electron discharge in a parallel-plate dielectric-loaded waveguide," *IEEE Electron Device Lett.*, vol. 27, no. 7, pp. 619–621, Jul. 2006.
- [8] D. Raboso, "Introduction to high power RF breakdown effects and PIM," presented at Workshop WM-02 High Power RF Breakdown and PIM in Space Applications, 48th Eur. Microw. Conf., Madrid, Spain, Sep. 2018.
- [9] M. Yu, "Power-handling capability for RF filters," *IEEE Microw. Mag.*, vol. 8, no. 5, pp. 88–97, Oct. 2007.
- [10] J. Uher, J. Bornemann, and U. Rosenberg, *Waveguide Components for Antenna Feed Systems: Theory and CAD*. Norwood, MA, USA: Artech House, 1993.
- [11] R. J. Cameron, C. M. Kudzia, and R. R. Mansour, *Microwave Filters for Communication Systems: Fundamentals, Design, and Applications*, 2nd ed. Hoboken, NJ, USA: Wiley, 2018.
- [12] J. V. Lebacqz, "High power klystrons," *IEEE Trans. Nucl. Sci.*, vol. 12, no. 3, pp. 86–95, Jun. 1965.
- [13] M. K. Joshi, N. Nayek, T. Tiwari, and R. Bhattacharjee, "Design and analysis of overmoded RF window for high-power applications in X-band," *IEEE Trans. Plasma Sci.*, vol. 48, no. 1, pp. 127–132, Jan. 2020.
- [14] J. Christensen, "ITU regulation for Ka-band satellite networks," Aug. 2012. [Online]. Available: https://www.itu.int/md/R12-ITURKA.BAND-C-0001/_page.print
- [15] H. Fenech, S. Amos, S. Tomatis, and V. Soumpholphakdy, "High throughput satellite systems: An analytical approach," *IEEE Trans. Aerosp. Electron. Syst.*, vol. 51, no. 1, pp. 192–202, Jan. 2015.
- [16] A. Woode and J. Petit, "Diagnostic investigations into the multipactor effect, susceptibility zone measurements and parameters affecting a discharge," European Space Agency, Noordwijk, The Netherlands, Tech. Rep. 1556, Nov. 1989.
- [17] R. Woo, "Final report on RF voltage breakdown in coaxial transmission lines," NASA, Jet Propulsion Lab, Pasadena, CA, USA, Tech. Rep. 32-1500, Oct. 1970.
- [18] *Multipaction Design and Test, European Cooperation for Space Standardization (ECSS)*, Standard ECSS-E-ST-20-01 C, 2020.
- [19] T. P. Graves, "Standard/handbook for multipactor breakdown prevention in spacecraft components," Aeorospace, El Segundo, CA, USA, Tech. Rep. TOR-2014-02198, May 2014.
- [20] AuroraSAT SPARK3D, 2021, Dassault Systèmes, Vélizy-Villacoublay, France, 2021. [Online]. Available: <https://www.3ds.com/products-services/simulia/products/spark3d>
- [21] CST, CST Studio Suite, 2021, Dassault Systèmes, Vélizy-Villacoublay, France, [Online]. Available: <https://www.3ds.com/products-services/simulia/products/cst-studio-suite>
- [22] A. Al-Mudhafar, J. Puech, and H. Hartnagel, "Investigation of multipactor effect in microwave components in the presence of fringing fields," in *Proc. 44th Eur. Microw. Conf.*, Rome, Italy, Oct. 2014, pp. 406–409, doi: [10.1109/EuMC.2014.6986456](https://doi.org/10.1109/EuMC.2014.6986456).
- [23] S. Anza *et al.*, "Recent developments on FEST3D/SPARK3D simulation tools," in *Proc. Int. Workshop Multipactor, Corona Passive Intermodulat. Space RF Hardware*, Valencia, Spain, Sep. 2014.
- [24] F. Teberio *et al.*, "Waveguide band-pass filter with reduced sensitivity to fabrication tolerances for Q-band payloads," in *Proc. IEEE MTT-S Int. Microw. Symp.*, Honolulu, HI, USA, Jun. 2017, pp. 1464–1467, doi: [10.1109/MWSYM.2017.8058897](https://doi.org/10.1109/MWSYM.2017.8058897).
- [25] P. Martín-Iglesias, F. Teberio, and M. A. G. Laso, "Analysis of the multipactor effect with linear frequency modulated signals," in *Proc. IEEE MTT-S Int. Conf. Numer. Electromagn. Multiphys. Model. Optim.*, Reykjavik, Iceland, Aug. 2018, pp. 1–4, doi: [10.1109/NEMO.2018.8503139](https://doi.org/10.1109/NEMO.2018.8503139).
- [26] J. Vague *et al.*, "Multipactor effect characterization of dielectric materials for space applications," *IEEE Trans. Microw. Theory Techn.*, vol. 66, no. 8, pp. 3644–3655, Aug. 2018.
- [27] F. Teberio, P. Martín-Iglesias, I. Arregui, I. Arnedo, T. Lopetegui, and M. A. G. Laso, "Compact harmonic rejection filter for C-band high-power satellite applications," in *Proc. IEEE MTT-S Int. Microw. Symp.*, Los Angeles, CA, USA, Aug. 2020, pp. 591–594, doi: [10.1109/IMS30576.2020.9224052](https://doi.org/10.1109/IMS30576.2020.9224052).
- [28] Ansys, HFSS, Canonsburg, PA, 2021. [Online]. Available: <https://www.ansys.com/products/electronics/ansys-hfss>
- [29] S. V. Langellotti, N. M. Jordan, Y. Y. Lau, and R. M. Gilgenbach, "CST particle studio simulations of coaxial multipactor and comparison with experiments," *IEEE Trans. Plasma Sci.*, vol. 48, no. 6, pp. 1942–1949, Jun. 2020.
- [30] J. Vague *et al.*, "Experimental validation of multipactor effect for ferrite materials used in L- and S-band nonreciprocal microwave components," *IEEE Trans. Microw. Theory Techn.*, vol. 67, no. 6, pp. 2151–2161, Aug. 2019.
- [31] G. Torregrosa, A. Coves, B. Gimeno, I. Montero, C. Vicente, and V. E. Boria, "Multipactor susceptibility charts of a parallel-plate dielectric-loaded waveguide," *IEEE Trans. Electron Devices*, vol. 57, no. 5, pp. 1160–1166, May 2010.
- [32] D. Gonzalez-Iglesias *et al.*, "Multipactor susceptibility charts for ridge and multiridge waveguides," *IEEE Trans. Electron Devices*, vol. 59, no. 12, pp. 3601–3607, Dec. 2012.
- [33] *Multipactor Handbook, European Cooperation for Space Standardization (ECSS)*, Standard ECSS-E-HB-20-01A, 2020.
- [34] C. Ernst, V. Postoyalko, and N. G. Khan, "Relationship between group delay and stored energy in microwave filters," *IEEE Trans. Microw. Theory Techn.*, vol. 49, no. 1, pp. 192–196, Jan. 2001.
- [35] A. E. Atia and A. E. Williams, "New types of bandpass filters for satellite transponders," *COMSAT Tech. Rep.*, vol. 1, no. 1, pp. 21–43, Nov. 1971.
- [36] F. De Paolis and F. Frezza, "Simplified prediction of peak power-handling capability for stepped-impedance low-pass filters," *IEEE Trans. Microw. Theory Techn.*, vol. 61, no. 3, pp. 1079–1085, Mar. 2013.
- [37] J. R. M. Vaughan, "A new formula for secondary emission yield," *IEEE Trans. Electron Devices*, vol. 36, no. 9, pp. 1963–1967, Sep. 1989.
- [38] C. Vicente *et al.*, "Multipactor breakdown prediction in rectangular waveguide based components," in *Proc. IEEE MTT-S Int. Microw. Symp. Dig.*, Long Beach, CA, USA, Jun. 2005, pp. 1055–1058, doi: [10.1109/MWSYM.2005.1516852](https://doi.org/10.1109/MWSYM.2005.1516852).
- [39] J. Lara *et al.*, "Multipactor prediction for on-board spacecraft RF equipment with the MEST software tool," *IEEE Trans. Plasma Sci.*, vol. 34, no. 2, pp. 476–484, Apr. 2006.
- [40] A. Taflové and S. C. Hagness, *Computational Electrodynamics: The Finite-Difference Time-Domain Method*, 3rd ed. Norwood, MA, USA: Artech House, 2005.
- [41] E. Sorolla, A. Sounas, and M. Mattes, "Space charge effects for multipactor in coaxial lines," *Phys. Plasmas*, vol. 22, no. 3, Mar. 2015, Art. no. 033512.
- [42] *Multipactor & Breakdown Analysis of RF Components*, CST Webinar, Nov. 2015.

- [43] M. Yu, A. Panariello, M. Ismail, and J. Zheng, "Passive 3-D simulators," *IEEE Microw. Mag.*, vol. 9, no. 6, pp. 50–61, Dec. 2008.
- [44] M. A. Furman and M. T. F. Pivi, "Probabilistic model for the simulation of secondary electron emission," *Phys. Rev. ST Accel. Beams*, vol. 5, Dec. 2002, Art. no. 124404.
- [45] R. Udiljak, D. Anderson, M. Lisak, V. E. Semenov, and J. Puech, "Multipactor in a coaxial transmission line Part I. Analytical study," *Phys. Plasmas*, vol. 14, no. 3, Mar. 2007, Art. no. 033508.
- [46] N. M. Jordan, F. B. Darby, S. V. Langellotti, Y. Y. Lau, and R. M. Gilgenbach, "Coaxial multipactor susceptibility at GHz frequencies," in *Proc. IEEE Int. Vac. Electron. Conf., Busan*, South Korea, Apr. 2019, pp. 1–2, doi: [10.1109/IVEC.2019.8744872](https://doi.org/10.1109/IVEC.2019.8744872).
- [47] V. E. Semenov, N. Zharova, R. Udiljak, D. Anderson, M. Lisak, and J. Puech, "Multipactor in a coaxial transmission line Part II. Particle-in-cell simulations," *Phys. Plasmas*, vol. 14, no. 3, Mar. 2007, Art. no. 033509.
- [48] A. M. Perez *et al.*, "Prediction of multipactor breakdown thresholds in coaxial transmission lines for traveling, standing, and mixed waves," *IEEE Trans. Plasma Sci.*, vol. 37, no. 10, pp. 2031–2040, 2009.
- [49] ESA-ESTEC, ECSS Multipactor Tool, Noordwijk, The Netherlands: European Space Agency, 2021. [Online]. Available: <https://www.val-space.com/en/ecss-multipactortool/>
- [50] A. E. Atia and A. E. Williams, "Narrow-bandpass waveguide filters," *IEEE Trans. Microw. Theory Techn.*, vol. 20, no. 4, pp. 258–265, Apr. 1972.
- [51] A. Atia, A. Williams, and R. Newcomb, "Narrow-band multiple-coupled cavity synthesis," *IEEE Trans. Circuits Syst.*, vol. 21, no. 5, pp. 649–655, Sep. 1974.
- [52] R. J. Cameron, "General coupling matrix synthesis methods for Chebyshev filtering functions," *IEEE Trans. Microw. Theory Techn.*, vol. 47, no. 4, pp. 433–442, Apr. 1999.
- [53] O. Monerris *et al.*, "High power RF discharge detection technique based on the in-phase and quadrature signals," *IEEE Trans. Microw. Theory Techn.*, vol. 69, no. 12, pp. 5429–5438, Dec. 2021, doi: [10.1109/TMTT.2021.3120657](https://doi.org/10.1109/TMTT.2021.3120657).



PABLO GONZÁLEZ was born in Gandia, Spain, in 1994. He received the B.Sc. degree in physics from the Universitat de València, Valencia, Spain, the M.Sc. degree in telecommunication engineering in 2018 from the Universitat Politècnica de València, Valencia, Spain where he is currently working toward the Ph.D. degree in telecommunication engineering.

In 2019, he joined the Departamento de Comunicaciones, Universitat Politècnica de València. His current research interests include the analysis and

design of passive components in waveguide technology for space applications and high-power RF effects.

Mr. González was the recipient of the 2018 FPU Fellowship from the Ministerio de Universidades, Spanish Government.



CARLOS ALCAIDE received the M.Sc. and Ph.D. degrees in telecommunication engineering from the Universitat Politècnica de València (UPV), Valencia, Spain, in 2012 and 2019, respectively.

In 2019, he joined the Institute of Telecommunications and Multimedia Applications, UPV. His current research interests include the analysis and design of passive components for space applications and high-power RF effects.



RAÚL CERVERA was born in Valencia, Spain, in 1998. He received the B.Sc. degree in telecommunication engineering from the Universitat Politècnica de Valencia, Valencia, Spain, in 2020. He is currently working toward the double M.Sc. degree in telecommunication engineering.

Since 2021, he has been a Junior Researcher with Val Space Consortium, Valencia, Spain. His current research interests include passive RF components, electromagnetic analysis, and RF breakdown power effects.



MIGUEL RODRÍGUEZ was born in Valencia, Spain in September 1998. He received the B.Sc. degree in telecommunication engineering in 2020 from the Universitat Politècnica de València (UPV), Valencia, where he is currently working toward the M.Sc. degree in telecommunications technologies, systems, and networks, and the M.Sc. degree in telecommunications engineering.

In 2021, he joined Val Space Consortium, Valencia, Spain, as a Junior Researcher. His current research interests include multipactor prediction techniques and RF breakdown phenomena.



ÓSCAR MONERRIS received the M.Sc. degree in electric engineering from the Universitat Politècnica de València, Valencia, Spain, in 2008, and coursed the specialization M.Sc. degree in 2009, and the M.Sc. degree in economics from the Universitat de València, Valencia, Spain, in 2014.

In 2010, he joined Val Space Consortium, Valencia, Spain, as a Technical Staff. His current research interests include high RF power effects in space applications, focusing in the analysis, testing, and detection of the RF breakdown in the

presence of multicarrier and modulated signals. Since 2020, he has been a Member of Val Space Consortium Research and Development Board. Since 2016, he has also been a member of the Telecommunication Engineering Association in Valencia Board.



JOHN PETIT received the B.Sc. degree in physics from the University of Sussex, Brighton, U.K., in 1980.

Since then, he has been working for a range of companies and institutions, covering the areas of defense, research, mobile systems, and space technology, which has included working with the Marconi Company, Stanmore, U.K., University of Kent, Canterbury, U.K., COM DEV, Aylesbury, U.K., Honeywell U.K. and ESTEC, Noordwijk, The Netherlands. He is currently a Senior Researcher with Val Space Consortium, Valencia, Spain, where he is responsible

for overseeing a three-year project funded by ESA, investigating multipactor prediction techniques in relation to GNSS signals. His principal experience is in the field of high power discharge effects, such as multipactor and gas breakdown in space components.

Mr. Petit is a member of the Institution of Engineering and Technology, U.K.



ANA RODRÍGUEZ (Member, IEEE) was born in Lugo, Spain. She received the M.Sc. degree in telecommunications engineering from the Universidade de Vigo, Vigo, Spain, in 2008, the M.Sc. and Ph.D. degrees in telecommunications engineering from the Universitat Politècnica de València (UPV), València, Spain, in 2010 and 2014, respectively. She participated in the Erasmus Exchange Program, developing her M.Sc. thesis with the University of Oulu, Oulu, Finland.

Since 2008, she has been with the Institute of Telecommunications and Multimedia Applications, UPV. Her current research interests include the CAD design of microwave devices (planar and waveguide), additive manufacturing, and EM optimization methods.



ANA VIDAL (Member, IEEE) was born in Valencia, Spain, in 1970. She received the Telecommunications Engineer degree from the Universidad Politècnica de Valencia, Valencia, Spain. She stayed one year with the University of Strathclyde, Glasgow, U.K., under the Erasmus International Exchange Program. In 1993, she was involved in broadband communications development in the main research center of Telecom Portugal. She then became a Research Assistant with the Universidad Politècnica de Valencia. In 1995 and 1996, she held

a Spanish Trainee position with the European Space Research and Technology Centre (ESTEC)–European Space Agency (ESA), Noordwijk, The Netherlands, where she was involved in the study and implementation of software for synthetic aperture radar (SAR) image processing. In 1996, she returned to the Universidad Politècnica de Valencia, where she held several lecturing positions, and became an Associate Professor in 2001. Her current research interests include remote sensing data classification, GNSS algorithms, and numerical methods for microwave structures analysis, including the wavelet transform.



JOAQUÍN VAGUE was born in Valencia, Spain, in 1970. He received the M.Sc. degree in electronic engineering from the Universitat de València, Valencia, Spain, in 2003. He is currently working toward the Ph.D. degree in electronic engineering.

He is currently a Technical Researcher in charge of several Laboratories with the Departamento de Comunicaciones, Universitat Politècnica de València, Valencia, Spain. His current research interests include the design of microwave passive devices, especially in filters and nonreciprocal devices and the improvement in manufacturing processes in the RF and microwave range.



JOSÉ V. MORRO (Member, IEEE) was born in Segorbe, Castellón, on April 3, 1978. He received the Ingeniero de Telecomunicación and Doctor Ingeniero de Telecomunicación degrees from the Universitat Politècnica de València, València, Spain, in 2001 and 2011, respectively.

In 2001, he became a Research Assistant with the Universitat Politècnica de València. In 2003, he joined the Area de Teoría de la Señal y Comunicaciones, Universidad Miguel Hernández de Elche, where he was a Lecturer during 2003–2005. In

2005, he rejoined the Departamento de Comunicaciones, Universitat Politècnica de València, where he was as an Assistant Lecturer during 2005–2007, a Lecturer, and since 2016 he has been an Assistant Professor. His current research interests include synthesis and automated design of passive components in waveguide, planar and hybrid technologies, additive manufacturing, and EM optimization methods.



PABLO SOTO (Member, IEEE) was born in Cartagena, Spain, in 1975. He received the M.Sc. and Ph.D. degrees (*cum laude*) in telecommunication engineering from the Universidad Politècnica de València, Valencia, Spain, in 1999 and 2012, respectively.

In 2000, he joined the Departamento de Comunicaciones, Universidad Politècnica de València, where he has been an Associate Professor since 2012. In 2000, he was an European Union Research Fellow with the European Space Research

and Technology Centre, European Space Agency (ESTEC-ESA), Noordwijk, The Netherlands. His current research interests include numerical methods for the analysis, synthesis, and fully automated design of passive components in waveguide and planar technologies, the development and design of novel hardware for satellite applications, and high-power RF effects.



VICENTE E. BORIA (Fellow, IEEE) was born in Valencia, Spain, in May 1970. He received the Ingeniero de Telecomunicación (Hons.) and Doctor Ingeniero de Telecomunicación degrees from the Universidad Politècnica de Valencia, Valencia, Spain, in 1993 and 1997, respectively.

In 1993, he joined the Departamento de Comunicaciones, Universidad Politècnica de Valencia, where he has been a Full Professor since 2003. In 1995 and 1996, he was holding a Spanish Trainee position with European Space Research and

Technology Centre, European Space Agency (ESTEC-ESA), Noordwijk, The Netherlands, where he was involved in the area of EM analysis and design of passive waveguide devices. He has authored or coauthored 15 chapters in technical textbooks, 200 papers in refereed international technical journals, and more than 250 papers in international conference proceedings. His current research interests include the analysis and automated design of passive components, left-handed and periodic structures, and also on the simulation and measurement of power effects in passive waveguide systems.

Dr. Boria has been a member of the IEEE Microwave Theory and Techniques Society (IEEE MTT-S) and the IEEE Antennas and Propagation Society (IEEE AP-S) since 1992. He is also a member of the European Microwave Association (EuMA), and is the Chair of the 48th European Microwave Conference held in Madrid, Spain. He is a reviewer of several IEEE and IET technical journals in his areas of interest. He was an Associate Editor for IEEE MICROWAVE AND WIRELESS COMPONENTS LETTERS during 2013–2018 and IET Electronics Letters during 2015–2018. He is currently the Subject Editor (Microwaves) of IET Electronics Letters, and an Editorial Board Member of International Journal of RF and Microwave Computer-Aided Engineering. He is also a member of the Technical Committees of the IEEE-MTT International Microwave Symposium and of the European Microwave Conference.